



Single metal atom oxide anchored Fe₃O₄-ED-rGO for highly efficient photodecomposition of antibiotic residues under visible light illumination

Karuppaiah Selvakumar^{a,1}, Yueshuai Wang^{a,1}, Yue Lu^{a,*}, Bohai Tian^a, Zeyu Zhang^a,
Jingcong Hu^a, Annamalai Raja^b, Muthuraj Arunpandian^c,
Meenakshisundaram Swaminathan^{c,*}, Hongxing Dai^d, Manling Sui^{a,*}

^a Institute of Microstructure and Properties of Advanced Materials, Faculty of Materials and Manufacturing, Beijing University of Technology, Beijing 100124, China

^b Department of Chemistry, College of Natural Sciences, Yeungnam University, Gyeongsan, Gyeongbuk 38541, Republic of Korea

^c Nanomaterials Laboratory, Department of Chemistry, Kalasalingam Academy of Research and Education, Krishnankoil, 626126, India

^d Laboratory of Catalysis Chemistry and Nanoscience, Department of Chemistry and Chemical Engineering, College of Environmental and Energy Engineering, Beijing University of Technology, Beijing 100124, China

ARTICLE INFO

Keywords:

Single metal atom oxide
Photodegradation
Ciprofloxacin
Ibuprofen
Magnetic nanocomposite

ABSTRACT

Designing highly efficient photocatalysts is significantly important to degrade the harmful pollutions in water. In this study, photocatalyst of Fe₃O₄-ED-rGO with dissolved HPV was successfully prepared and electron microscopy characterization revealed that large number of single tungsten/vanadium atom oxide (ST/VAO) was homogeneously deposited on Fe₃O₄ nanoparticles in SMAO-MrGO-ED sample and occupied the bivalent Fe²⁺ sites. Meanwhile, phase analysis confirmed that the Fe₃O₄ nanocomposites were mostly converted from the reduced Fe₂O₃ by the hydrolysis of rGO-ED-HPV. Such a highly dispersed monatomic adsorption on the bivalent Fe²⁺ of polycrystalline SMAO-MrGO-ED nanocomposite not only benefits for the visible light absorption from 2.7 eV to 2.10 eV, but also offers abundantly active sites to get the highest activity of 98.43% and 98.12% for ciprofloxacin (CF) and ibuprofen (IBF) photodegradation, respectively. All these discoveries give us a new insight to design the photocatalysts with high photodegradation efficiency, low cost, short reaction time and good reusability.

1. Introduction

Human and veterinary drugs, personal care products such as sunscreens and cosmetics are included in the list of hazardous chemicals because of their impact on human health [1,2]. These compounds mainly enter into the natural water environment through the discharge of sewage to river sediments, surface soil and groundwater [3]. In addition, these chemicals are most dangerous to human and aquatic life due to their toxicity to induce endocrine disorder and antibiotic resistance [4,5]. For example, Ciprofloxacin (CF), as a fluoroquinolone antibiotic, has been used extensively in human and animal treatment [6,7]. However, the threshold concentration of CF in wastewater treatment plant (WWTP) is in the range of 313–568 ng L⁻¹ [8] and 124.5 µg L⁻¹ in raw sewage hospital water [9], and this bactericidal drug could only be detrimental after a long-time degradation even at a low concentration. Besides, increased using and exposing to antibiotics over the past

decades have enhanced the bacterial resistance against them [10,11]. Meanwhile, Ibuprofen (IBF) is commonly used as another non-steroidal anti-inflammatory drug for body pain, fever and rheumatoid arthritis [12], and this chemical can be frequently found in affluent, surface water and groundwater with a mean concentration of 8, 0.24 and 0.024 µg L⁻¹, respectively [13]. While, in some parts of the world, a presence of 5–25 ng L⁻¹ of IBF in drinking water has been reported [14]. In order to remove the CF and IBF, some methods like sedimentation, flocculation, coagulation, filtration and chlorination have been developed, however, these methods are normally inefficient and purification partially [15,16]. Thus, the removal of CF and IBF from the waste water requires a more efficient treatment system [5].

Recently, Advanced Oxidation Processes (AOPs) have been widely applied to decompose these hazardous pharmaceutical organic pollutants. Among AOPs materials, semiconductor photocatalysts, such as various metal oxides TiO₂ [17], ZnO [18], Fe₂O₃ [19] and coupled

* Corresponding authors.

E-mail addresses: luyue@bjut.edu.cn (Y. Lu), m.swaminathan@klu.ac.in (M. Swaminathan), mlsui@bjut.edu.cn (M. Sui).

¹ The authors are equal contribution.

materials γ -Fe₂O₃/black-TiO₂ [20], NiS/MoS₂/C₃N₄ [21], Ag@PCNS/BiVO₄ [22], Ce³⁺/Ce⁴⁺-Fe₃O₄ [23], 3D tripyramid TiO₂ [24], WO₃/Fe₃O₄ [25], TiO₂/ γ -Fe₂O₃/GO [26], g-C₃N₄/Fe₃O₄/BiOI [27] and TiO₂NTs/Fe₃O₄ [28], have been utilized to degrade most of the organic pollutants (organic dyes and pharmaceutical compounds) by oxidizing them with photogenerated highly active reactive oxygen species (ROS), such as superoxide radicals (O₂[•]), hydroxyl radicals ([•]OH) [29–33]. However, due to the aggregation of these metal oxide nanoparticles, the active surface area on photocatalysts under visible light is limited [34], which further restricts their application in photocatalysis.

In order to settle this problem, capping on conductive supporting materials (such as carbon, graphene, C₃N₄ etc.) and reducing the size of metal oxides into single-atom catalysts (SACs), such as FeO_x, α -Ni(OH)₂, is a good strategy to improve their photoactivity. The isolated metal oxide atoms are deposited on the surface of supported materials without commendable interaction among these monodispersed metal atoms [35–38]. Meanwhile, the properties present in the single-atom catalysts are ultimately improved by increasing the density of active catalytic sites and reducing the oxide dimension and metal size to their limit [36]. Unfortunately, until today, it is still very difficult to generate a high density of single metal atom oxide (SMAO) on the catalysts, especially at a high synthesis temperature due to its instability, which makes the wide application of SACs to be a great challenge [37].

Here, we demonstrated a new method to develop a high number density of single metal atom oxides on the magnetic iron oxide (M: Fe₃O₄), reduced graphene oxide (rGO), ethylene diamine (ED) and HPV (HPV: H₄[PVW₁₁O₄₀].32H₂O) composite, which was successfully applied to photodegradation of ciprofloxacin and ibuprofen under simulated visible light illumination. The advantage of this magnetic catalyst is that it can be easily separated from the external magnet and easily recycled from the reactive medium field [25]. Simultaneously conversion of Fe₂O₃ into Fe₃O₄ nanoparticles takes place under the reaction of reduced graphene oxide (rGO)/ethylene diamine/HPV components by produced electrons. During the conversion from Fe₂O₃ into Fe₃O₄, the configuration of single tungsten atom oxide (STAO)/single vanadium atom oxide (SVAO) has been formed on the metal oxides, which achieves a higher density of single catalytic active sites.

2. Experimental

2.1. Materials and methods

Graphite, Fe₃O₄, FeCl₃·6H₂O, ethylene glycol, Na₂HPO₄, NaVO₃, Na₂WO₄·2H₂O, and H₂SO₄ were purchased from Sigma Aldrich, and diethyl ether, ethanol, ethylene diamine, Ciprofloxacin and Ibuprofen were obtained from Merck, India. All chemicals were used without further purification. UV diffuse reflectance spectrum (UV-DRS) of the samples were obtained by UV-2450, Shimadzu spectrophotometer. Fourier Transform Infrared Spectrometer (FT-IR) were recorded using Shimadzu, IR Tracer-100, FT-IR spectrophotometer. Photoluminescence (PL) spectra were recorded by Perkin Elmer LS 55 fluorescence spectrometer. The valance bands (VB) of photocatalysts were evaluated from Ultraviolet Photoelectron Spectroscopy, UPS PHI 5000 Versaprobe III X. The surface morphology of composite materials was observed by scanning electron microscope, Helios Nanolab 600i, operated at an acceleration voltage of 30 kV. BRUKER X-ray Diffraction (XRD) D8 ADVANCE instrument was used for taking structural data. High angle annular dark field- Scanning Transmission Electron Microscopy (HAADF-STEM) images and nanobeam diffraction (NBD) patterns of the photocatalyst were taken using FEI Titan G2 transmission electron microscope (TEM) with 300 kV accelerating voltage. The elementary concentration in SMAO-MrGO-ED was measured by the inductively coupled plasma optical emission spectrometer (ICP-OES) (Optima 7300 DV, PerkinElmer). In addition, the X-ray absorption fine structure (XAFS) results were performed at beamline 1W2B of the Beijing Synchrotron Radiation Facility in fluorescence mode using a fixed-exit Si(111) double crystal

monochromator. Then, the XAFS raw data were background-subtracted, normalized and Fourier transformed by the standard procedures with the IFEFFIT package. The oxidation state of elements present in the nanocomposites material was analyzed by X-ray photoelectron spectroscopy (XPS), PHI Quantum 2000. The concentration of organic pollutants was obtained using UV-visible spectrophotometer (UV-1800, Shimadzu). Electron spin resonance (ESR) spectra were obtained using a Bruker model A300 spectrometer with a Philip lamp of 254 nm as light source, and 5,5-dimethyl-L-pyrroline-N-oxide (DMPO) as trapper. The sample is dispersed in purified methanol for the detection of O₂[•]. The electrochemical impedance spectroscopy (EIS), transient photocurrent response were measured on the electrochemical workstation (Corrtest CS350H). The electrochemical workstation was a standard three-electrode system, in which the catalyst-coated glassy carbon was the working electrode, the carbon rod was the counter electrode and the saturated calomel electrode was the reference electrode. A 500 W Xe arc lamp equipped with a 420 nm cutoff filter was utilized as a light source. EIS spectra was recorded over the frequency range from 0.1 Hz to 100 kHz. The scanning rate of LSV curve is 5 mV/s.

2.2. Sample preparation

2.2.1. Preparation of magnetic reduced graphene oxide (MrGO/Fe₂O₃-rGO) and MrGO-ED

Magnetic reduced graphene oxide was prepared from GO nano-sheets, FeCl₃·6H₂O and sodium sulphite as per the procedure reported [39]. MrGO-ED was prepared with 0.3 g of MrGO in a solution of 20 mL ethylene glycol and 40 mL ethylene diamine by sonication and solvothermal method as described elsewhere [39].

2.2.2. Preparation of heteropoly-11-tungsto-1-vanadophosphoric acid (H₄[PVW₁₁O₄₀].32H₂O)

Heteropoly-11-tungsto-1-vanadophosphoric acid was prepared by the modified procedure [40]. In a typical procedure, 0.71 g of disodium hydrogen phosphate (Na₂HPO₄) dissolved in 10 mL of water was mixed with 0.61 g of sodium metavanadate (NaVO₃) dissolving in 10 mL of boiling water. The mixture was cooled to room temperature and acidified with 1 mL conc. sulfuric acid, which turned into a red color solution. 17.76 g of sodium tungstate dihydrate (Na₂WO₄·2H₂O) dissolved in 20 mL of water was added to the reaction mixture and 8.4 mL of conc. sulfuric acid was added slowly with vigorous stirring while the dark red color was faded. The HPV was then extracted using 80 mL of diethyl ether and separated as heavy oily etherate (bottom layer) followed by evaporation in a vacuum desiccator. H₄[PVW₁₁O₄₀].32H₂O was obtained as crystalline yellow solid.

2.2.3. Synthesis of SMAO-MrGO-ED

The catalysts with different HPV concentration-*x* (*x* = 10, 20, 30 wt %) were prepared by a hydrothermal treatment. The MrGO-ED (0.8 g) was added to 10 mL ethanol with stirring for 30 min. The corresponding amount of H₄[PVW₁₁O₄₀] dissolved in a mixture of ethanol (20 mL) and H₂O (10 mL) was added dropwise. The amounts of H₄[PVW₁₁O₄₀] used to obtain solid materials with *x* = 10%, 20% and 30% mass percentages of heteropoly acid were 0.1 g, 0.2 g and 0.3 g, respectively. The resulting reaction mixture was stirred for 5 h at room temperature, then transferred into a Teflon autoclave and maintained for 12 h in 180 °C. The final solid material was recovered by filtration, washed several times with distilled water/ethanol and dried in air for 12 h at 100 °C (Fig. 1a).

2.3. General procedure for photodegradation of CF and IBF pollutants

Photodegradation efficiencies of the catalysts with three different concentrations (10, 20 and 30 wt%) of HPV were tested by the CF degradation (Fig. S1), from which we could find that catalyst with 20 wt % HPV loading on the MrGO-ED takes the highest photo-activity. Herein, the 20 wt% HPV loaded MrGO-ED sample in this text was

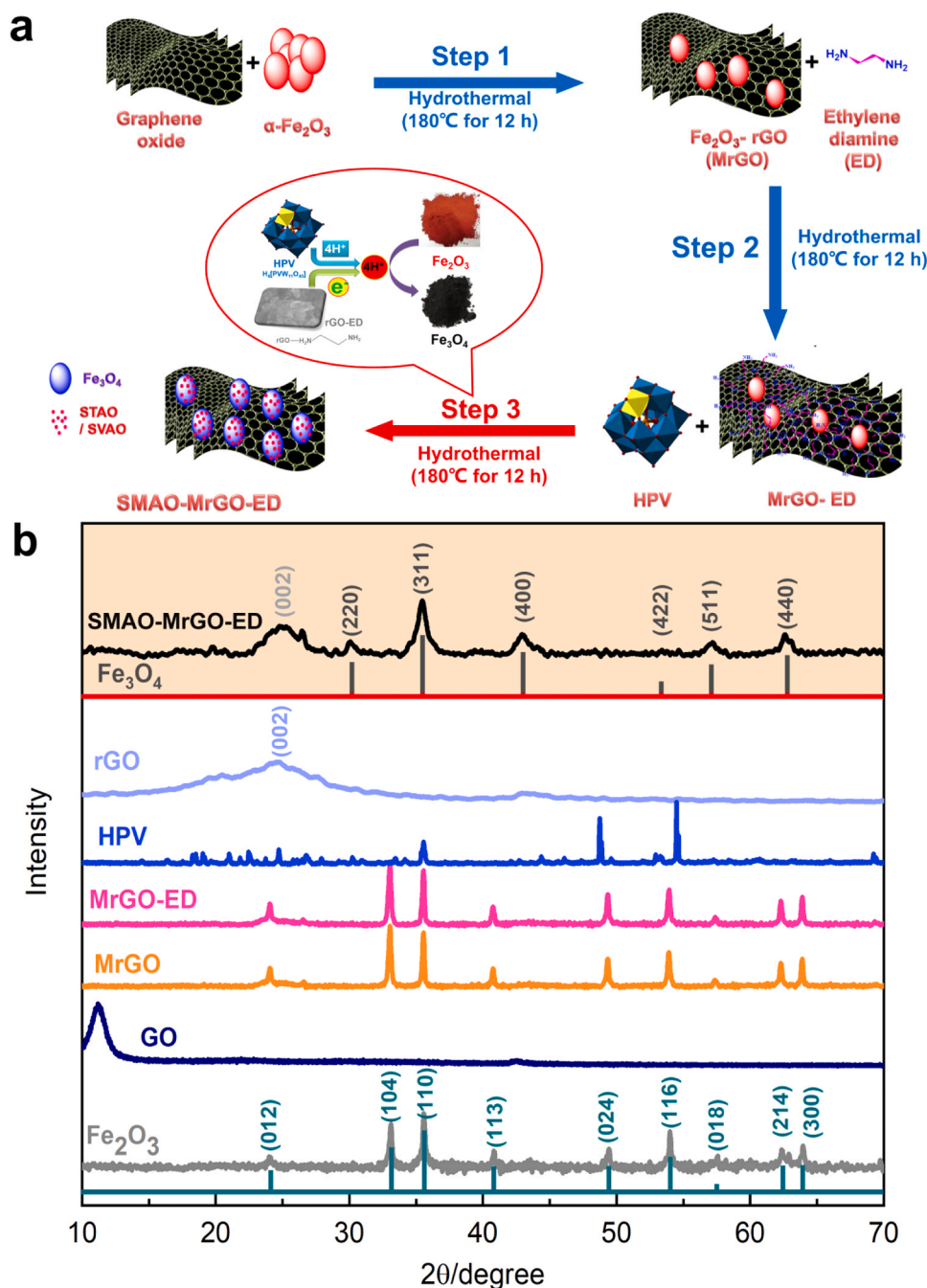


Fig. 1. a) Schematic illustration for the preparation of SMAO-MrGO-ED nanocomposite. Inset (red cycle area on the step 3) shows the reaction mechanism for the phase transition from Fe_2O_3 to Fe_3O_4 by mixing the rGO-ED, Fe_2O_3 and $\text{H}_4[\text{PVW}_{11}\text{O}_{40}]$ materials. During the synthesis of SMAO-MrGO-ED compound, rGO-ED can offer the electrons. Meanwhile, the electron would reduce the hydrogen ions in HPV into atomic hydrogen. Then, the atomic hydrogen has strong redox ability to reduce the Fe_2O_3 into Fe_3O_4 . b) X-ray powder diffraction pattern of Fe_2O_3 , GO, MrGO, MrGO-ED, HPV, rGO and SMAO-MrGO-ED nanocomposite. The XRD patterns of Fe_2O_3 , MrGO and MrGO-ED were assigned as Fe_2O_3 in accordance with the JCPDS card 33-0664. The Fe_2O_3 peaks are not presented in XRD patterns of SMAO-MrGO-ED and only can be characterized as Fe_3O_4 in accordance with the JCPDS card 19-0629 (the yellow background area).

named as “SMAO-MrGO-ED” and it was characterized comprehensively and utilized for the photodegradation of organic pollutants. While, for the photodegradation process of organic pollutants, 50 mg of the photocatalyst was dispersed in the 100 mL CF (concentration $40\ \mu\text{M}$) and IBF (concentration $20\ \mu\text{M}$) antibiotic solutions respectively, which was taken in 250 mL beaker. After magnetic stirring for 30 min in dark condition, the solution was shifted to a photoreactor vessel and irradiated by visible light (tungsten lamp- $150\ \text{mW}/\text{cm}^{-2}$). The sample was taken at an appropriate time interval, and after removing the catalyst by centrifugation, the concentration change of CF and IBF was measured. The concentration of CF and IBF antibiotic was estimated by their absorption at 276 and 224 nm by an UV-visible spectrophotometer.

3. Results and discussion

3.1. The design philosophy of SMAO-MrGO-ED materials

As one of the excellent AOP materials, Fe_3O_4 is the superior response to efficient photocatalyst and magnetic recoverable in the reaction medium [25]. The mixed-valence ($\text{Fe}^{\text{II}}\text{-Fe}^{\text{III}}$) presenting in the magnetite- Fe_3O_4 makes it to be an n-type semiconductor, which is non-toxic, low-cost materials and can be easily converted with desired properties [23]. However, until now, most of the synthesis methods for Fe_3O_4 from Fe_2O_3 photocatalysts are operated at the temperature ranging from 150°C to 500°C in H_2 atmosphere [41,42], and the disadvantage of these methods is that the conversion step requires both high temperature and explosive H_2 gas. In this work, we developed a method of preparing Fe_3O_4 nanoparticles directly at 180°C without H_2 gas.

Polyoxometalates (POMs) such as $H_4[PVW_{11}O_{40}]$ (HPV) compound are another typical representative for AOPs, which can form a wide class of discrete nano-sized transition metal-oxygen clusters. The POMs are commonly divided into two classes as heteropoly anions (HPA) and isopoly anions (IPA) [43]. Strongly acidic heteropoly anions with Keggin structure are remarkably stable on oxide surface. And HPA can act as an effective inorganic ion exchanger as they are strong bronsted acids. Besides, the photooxidation properties of HPA allow it to oxidize many organic-inorganic compounds directly through OH^\bullet radicals [43–45].

Besides, due to the large solubility of HPA or IPA into the water, they can form the ionic state and adsorb on the surface of supporting materials to form the SACs. Nowadays, the SACs have attracted considerable attention on heterogeneous catalysis as they provide advanced precious metal economy, enhance active site integrity and the ability to modify the inter-bonding between metal-support materials with strong control [44]. On the other hand, reduced graphene oxide (rGO) has been widely used as the supporting materials for photocatalysts due to its high surface area and strong electrical conductivity. The capping of rGO composites could also improve the polarization ability, dielectric properties and microwave attenuation performances [44]. So here, we just proposed that whether we could combine these materials together to form a highly dispersed adsorption sites of photocatalysts.

In this text, the $H_4[PVW_{11}O_{40}]$ compound as Keggin type heteropoly acid has been dissolved into water and we tried to bind on amine-functionalized Fe_3O_4 magnetite nanoparticles, which could be applied to photocatalytic degradation of dyes and oxidation of dibenzothiophene under UV irradiation [46,47]. Actually, surface modification of iron oxide has been largely used in biotechnology and catalysis as excellent supports for various catalysts because they can be easily separated and reused [48–50]. While, heteropoly acid supported on the iron oxide nanoparticles received much importance as active catalysts in the organic reactions [51–53,46,47]. In addition, amino functionalization is one of the most important modifications to form covalent bonds with functional groups on the surface of the modified material. This is often realized by the use of ethylene diamine (ED) coupling agent to generate terminal amino groups ($-NH_2$) on the surface of the semiconductor materials (Fe_3O_4) [39]. In order to enhance the bond between HPV and Fe_3O_4 nanoparticles, ED is mucilage on the surface of graphene oxide (GO) and co-coated on the Fe_3O_4 nanoparticle, which provides numerous amino groups as active absorption sites to enhance the absorption capacity of HPVs [39].

3.2. Phase analysis of the SMAO-MrGO-ED

After syntheses of the different composites step-by-step (Fig. 1a), they were identified by XRD. Fig. 1b shows the XRD patterns of Fe_2O_3 , GO, Fe_2O_3 -rGO (MrGO), Fe_2O_3 -rGO-ED (MrGO-ED), $H_4[PVW_{11}O_{40}]$ (HPV) and Fe_3O_4 -rGO-ED- $H_4[PVW_{11}O_{40}]$ (converted to SMAO-MrGO-ED), respectively. The XRD diffraction peaks of Fe_2O_3 (grey curve) at 23.98° , 32.97° , 35.57° , 40.51° , 49.16° , 53.80° , 57.20° , 62.23° , 63.88° can be indexed as (012), (104), (110), (113), (024), (116), (018), (214) and (300) corresponding to the pure Rhombohedral structure of Fe_2O_3 (JCPDS no. 33-0664) [54]. For the GO, the diffraction peak at 11.20° can be attributed to the graphene oxide (dark blue curve) [55]. The peak positions of Fe_2O_3 are unchanged after the formation of MrGO or MrGO-ED (yellow and pink curves). But the XRD peak of GO materials cannot be detected in the MrGO and MrGO-ED samples. In addition, it is interesting to find that the XRD peaks of SMAO-MrGO-ED (black curve) presented at 30.06° , 35.47° , 42.95° , 53.38° , 56.91° and 62.67° can be labeled as Fe_3O_4 (JCPDS no. 19-0629) but not Fe_2O_3 [56]. And the peak at 24.98° is corresponding to the (002) plane of the reduction of GO (rGO) (light blue curve) [57], while the HPV peaks (blue curve) are not observed in the XRD pattern of the final SMAO-MrGO-ED composite, which is mostly ascribe to the damage of HPV crystal structure after the dissolving of HPV during the sample preparation. So, based on the XRD results above in Fig. 1b, the phase transition from Fe_2O_3 into Fe_3O_4

during the formation of SMAO-MrGO-ED compounds has been confirmed.

3.3. Conversion mechanism of Fe_2O_3 into Fe_3O_4 nanomaterials

In order to understand the conversion mechanism from Fe_2O_3 into Fe_3O_4 during the synthesis of SMAO-MrGO-ED, we should firstly compare the XRD patterns of several compounds such as MrGO, MrGO-ED, Fe_2O_3 -HPV, HPV-rGO-ED, SMAO-MrGO-ED and (direct adding of Fe_3O_4) Fe_3O_4 /rGO/ED/HPV counterpart in Figs. 1b and S2. All the compounds were prepared by the same method as using for the synthesis of SMAO-MrGO-ED in Fig. 1a. For the compounds of MrGO, MrGO-ED, Fe_2O_3 -HPV and HPV-rGO-ED, the XRD peaks can only be labeled as Fe_2O_3 or HPV, and there is no conversion of Fe_2O_3 into Fe_3O_4 . But for the XRD peaks of SMAO-MrGO-ED, they match well with the Fe_3O_4 (red curves in Fig. 1b), which reveals that the conversion of Fe_2O_3 to Fe_3O_4 needs a synergetic effect between Fe_2O_3 , rGO, ED and HPV. Here, a four-step conversion mechanism of Fe_2O_3 to Fe_3O_4 nanomaterials during the formation of SMAO-MrGO-ED component is proposed (inset in Fig. 1a): i) the rGO-ED organic materials could produce electrons (e^-), which has the reduction ability [58]; ii) the $H_4[PVW_{11}O_{40}]$ component could supply abundant hydrogen ions (H^+) as the reaction medium [40]; iii) the electrons (e^-) and hydrogen ions (H^+) combine together to form the reduction agent of atomic hydrogen H^\bullet ; iv) the H^\bullet reacts with Fe_2O_3 materials under the high temperature ($180^\circ C$) and high pressure in Teflon autoclave for 12 h, which ensures the transformation into Fe_3O_4 nanomaterials [59]. It should be pointed out that Cardenas-Lizana et al. reported a partial reduction conversion for Fe_2O_3 into Fe_3O_4 could only be happened at hydrogenation atmosphere of $400^\circ C$ [56]. In this work, we get a new method to take a complete conversion of Fe_2O_3 into Fe_3O_4 at a low temperature of $\sim 180^\circ C$ and safety environment, which may be applicable to reduce other metal oxide materials.

3.4. Morphology evolution during the formation of SMAO-MrGO-ED

The morphology and composition of the as-prepared materials were firstly analyzed by using field emission scanning electron microscopy (FE-SEM). Initially, the Fe_2O_3 composite with fine nanostructures was segregated together, as shown in Fig. 2a. However, after the addition of rGO and ethylene diamine (ED) to synthesis MrGO-ED, the morphology of Fe_2O_3 has been changed into nanoclusters (diameter of 100–500 nm) and highly dispersed on the surface of thin wrinkled rGO materials (red arrow in Fig. 2b). While the surface morphology is slightly changed by support of HPV into SMAO-MrGO-ED (blue arrows in Fig. 2c and d), confirming the transition from Fe_2O_3 into Fe_3O_4 is mostly based on the morphology evolution of MrGO-ED. In addition, if we didn't add the GO and ED to synthesize the Fe_2O_3 -HPV, we could find that some HPV nanorods appear on the surface of compound (yellow arrow in Fig. S3b). Furthermore, if Fe_3O_4 is substituted for Fe_2O_3 to synthesize Fe_3O_4 /rGO/ED/HPV counterpart, the HPV nanorods (yellow arrows in Fig. S3c and d) still present apparently and separate from the Fe_3O_4 -rGO clusters, which is quite different from the morphology of SMAO-MrGO-ED (Figs. S3d and 2d). So, all these results confirm that during the synthesis of SMAO-MrGO-ED compounds, the added HPV nanorods have been completely dissolved and loaded on the surface of nanoparticles.

3.5. Identification of the single tungsten/vanadium atom oxides on SMAO-MrGO-ED

3.5.1. Characterization by the Cs corrected- transmission electron microscopy (TEM)

To check the adsorption state of HPV on SMAO-MrGO-ED, transmission electron microscopy (TEM) analysis of the compounds is shown in Figs. 2e and S4a. It can be found that the Fe_3O_4 nanoparticles were uniformly dispersed on the rGO layer (Fig. S4a) with an average diameter of approximately 12.5 nm (Fig. S4b). When we took the high angle

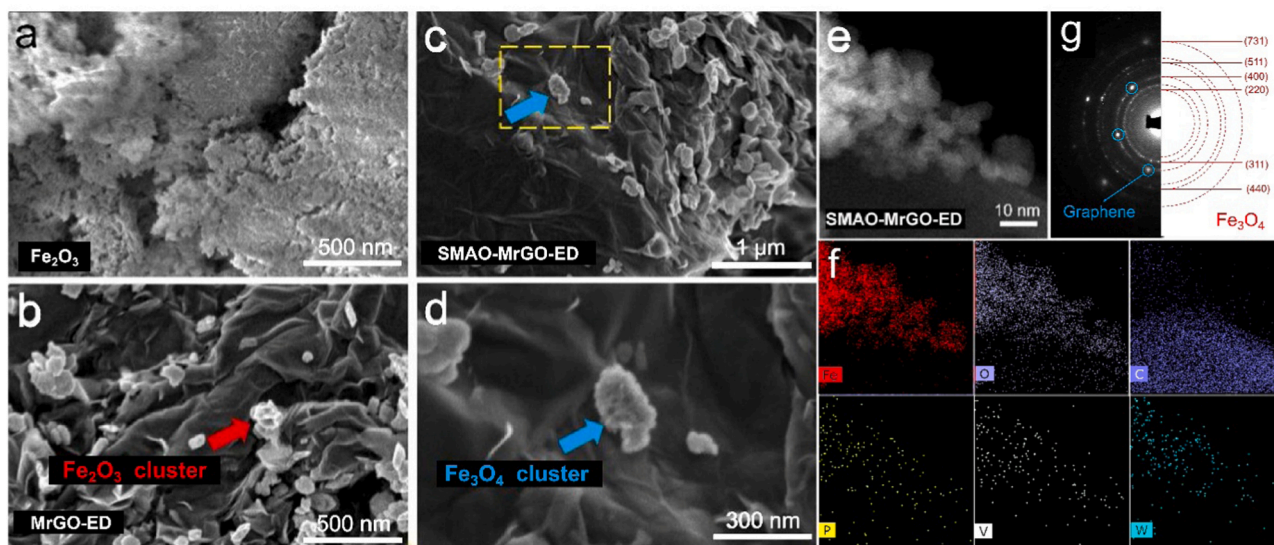


Fig. 2. Field emission scanning electron microscopy (FE-SEM) images of a) Fe_2O_3 , b) MrGO-ED, c) and d) SMAO-MrGO-ED nanocomposites (different magnification). The morphology of $\text{Fe}_2\text{O}_3/\text{Fe}_3\text{O}_4$ particles is with irregular shape in MrGO-ED, SMAO-MrGO-ED materials and highly dispersed on rGO. rGO is present as the substrate layer. e) STEM image of SMAO-MrGO-ED and f) the corresponding EDS mapping of the Fe, O, C, P, V, W elements in SMAO-MrGO-ED. g) Selected area electron diffraction (SAED) pattern of SMAO-MrGO-ED, red marks exhibit the polycrystalline Fe_3O_4 and the solid circles mark the diffraction spots of graphene.

annular dark-field (HAADF) images and energy dispersion spectrum (EDS) mapping of the SMAO-MrGO-ED compounds, it confirmed that the Fe_3O_4 nanoparticles were adsorbed on the surface of the rGO layer. Meanwhile, the W, V and P elementary (the composition of HPV) signals could also be detected, especially at the segregation areas of metal oxide

nanoparticles (Figs. 2f and S4c). Quantitative analysis on the atomic percentages of W, V and P elements on Fe_3O_4 are about 2.3 at%, 2.4 at% and 1.5 at% (Table S1), respectively. Meanwhile, the detection of inductively coupled plasma optical emission spectrometer (ICP-OES) confirms that elementary concentrations of SMAO-MrGO-ED

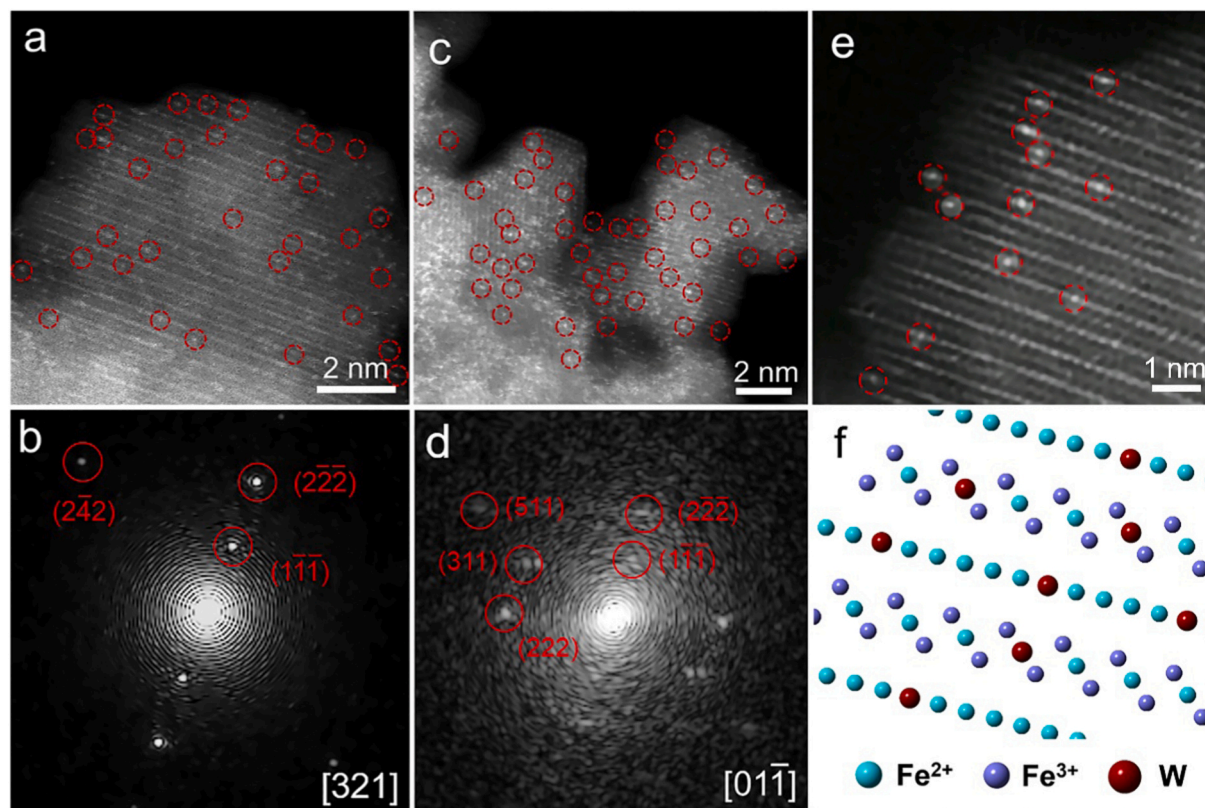


Fig. 3. a) and c) HAADF-STEM images of Fe_3O_4 nanoparticles in the SMAO-MrGO-ED nanocomposite, b) and d) the corresponding fast Fourier transform (FFT) patterns, respectively. e) High-resolution HAADF-STEM image of Fe_3O_4 nanoparticle along [321] direction, showing the presence of single tungsten atom oxide (STAO) on Fe_3O_4 in the SMAO-MrGO-ED materials, f) Simulation of the arrangement of W, Fe^{2+} and Fe^{3+} atoms in Fe_3O_4 observed along [321] direction, from which we can see that the W atoms are adsorbed on the bivalent Fe^{2+} atomic sites.

photocatalyst are 94.43 at%, 2.18 at%, 2.33 at% and 1.06 at% for Fe, W, V, and P elements (Table S2) respectively, which is very similar with the EDX result in Table S1. However, for such a concentration ratio of W and V, it is obviously inconsistent with the stoichiometric ratio of W, V and P elements in HPV ($\text{H}_4[\text{PVW}_{11}\text{O}_{40}]\cdot 32\text{H}_2\text{O}$), and all these results confirm that HPV has been dissolved and adsorbed on SMAO-MrGO-ED as the ionic form during the synthesis procedure. Furthermore, when analyzing the HAADF image and performing the selected area electron diffraction (SAED) pattern of SMAO-MrGO-ED in Fig. 2g, it confirmed that these metal oxide nanoparticles should be identified as Fe_3O_4 , while the hexagonal diffraction dots in SAED belong to the graphene layer substrate (blue circle in Fig. 2g).

As we all know, the intensity of HAADF image is approximately proportional to the square of the atomic number of the elements [35], here the atomic numbers of H, C, N, O, P, V, Fe, and W in SMAO-MrGO-ED compounds are 1, 6, 7, 8, 15, 23, 26 and 74, respectively. Based on this theory, the W atom with highest atomic number should take the brightest HAADF contrast. Besides that, a large number of bright contrast single atoms were deposited on the surface of Fe_3O_4 nanoparticles (Figs. 3a–e and S5), which are mostly assigned to the heavy element of W species. It should be pointed out that without the addition of HPV, no bright HAADF contrast of single atoms can be detected on the metal oxide in MrGO-ED as shown in Fig. S6b, which confirms that the highly dispersed P, V and W elements on metal oxides should come from the dissolving of HPV (Fig. S6e) during the synthesis

of SMAO-MrGO-ED. So, from the results above, we can conclude that the HPV compound has been dissolved into the solution, especially during the phase transition from Fe_2O_3 into Fe_3O_4 , meanwhile a large amount of single tungsten/vanadium oxide atoms are deposited on the surface of Fe_3O_4 in SMAO-MrGO-ED compounds.

3.5.2. Characterization by the extended X-ray absorption fine structure (EXAFS)

The coordination configuration of W and V atoms on SMAO-MrGO-ED was further confirmed by the extended X-ray absorption fine structure (EXAFS) spectra as shown in Fig. 4. Here, the WO_3 and W foil were taken as reference samples and the EXAFS spectra of W in SMAO-MrGO-ED is compared in Fig. 4a and b. The W-W coordination bond in W-foil appears at 2.59 Å (blue line in Fig. 4a), while the main peak of W-O coordination bond in WO_3 EXAFS spectrum (black line in Fig. 4a) locates at 1.36 Å. As compared with the EXAFS spectrum of SMAO-MrGO-ED (red line in Fig. 4a), absence of 2.59 Å peak for W-W bond reveals that there is no W cluster in the SMAO-MrGO-ED composites, while only the coordination peak of W-O bond appears at 1.40 Å [36]. At the same time, X-ray absorption near-edge structure (XANES) spectroscopy (Fig. 4b) also confirm that the coordination configuration of W in SMAO-MrGO-ED is very similar with the one in WO_3 (the broad white-line (WL) in both samples are at 10,210 eV, which corresponds to the electron transition from $2p_{3/2}$ to unoccupied W 5d-0 2p hybridized orbitals [60]). So, all the results above further confirms the

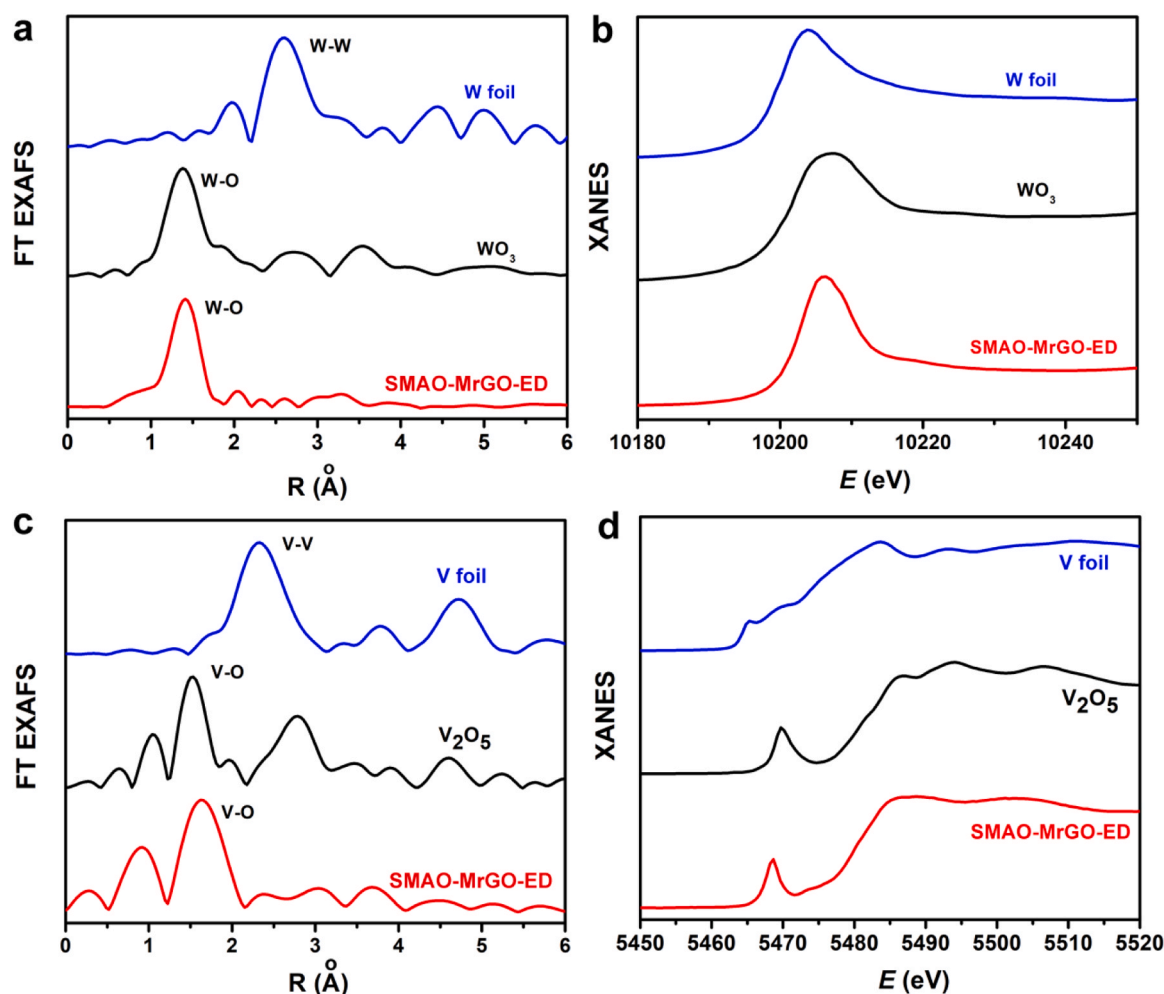


Fig. 4. a) The extended X-ray absorption fine structure (EXAFS) spectra of W–W and W–O bonds in W foil, WO_3 and SMAO-MrGO-ED samples, b) X-ray absorption near-edge structure (XANES) spectroscopy of W in W foil, WO_3 and SMAO-MrGO-ED samples, c) EXAFS spectra and d) XANES spectra of V in V foil, V_2O_5 and SMAO-MrGO-ED.

existence of W atoms as STAO anchoring on the Fe_3O_4 nanoparticles in SMAO-MrGO-ED photocatalyst, and this is consistent with the HAADF characterizations in Fig. 3. It is interesting to note that the main peak of V—O coordination bond in the EXAFS spectra of SMAO-MrGO-ED is at 1.62 Å (Fig. 4c), which is very close to the V—O coordination bond at 1.52 Å in V_2O_5 [61]. Meanwhile, for the XANES spectra of SMAO-MrGO-ED (Fig. 4d), a similar shape and maximum peak at 5470 eV could also be observed in the V_2O_5 reference sample [62], all these results confirm that SVAO also exists in the SMAO-MrGO-ED compounds.

3.5.3. Analyses of the chemical states of SMAO-MrGO-ED

In order to check the adsorption sites of heavy atoms on SMAO-MrGO-ED, here we simulated the atomic configuration projection of Fe_3O_4 (Figs. S7 and 3f) along the [321] zone axis, which benefits on the distinguishing of Fe^{2+} and Fe^{3+} sites in Fe_3O_4 lattice (Fig. S7). As shown in Fig. 3e and f, it is easy to find that almost all the bright HAADF contrast atoms are located at the bivalent Fe^{2+} sites (Fig. S8). As previous reports, Fe^{2+} played an important role in the photodegradation of Tetracycline due to solar light harvesting and rapid electron transport [20]. So here, the adsorption of single tungsten/vanadium atoms on the Fe^{2+} site may improve electron transport. Besides that, the chemical states of SMAO-MrGO-ED nanomaterials were analyzed by XPS as

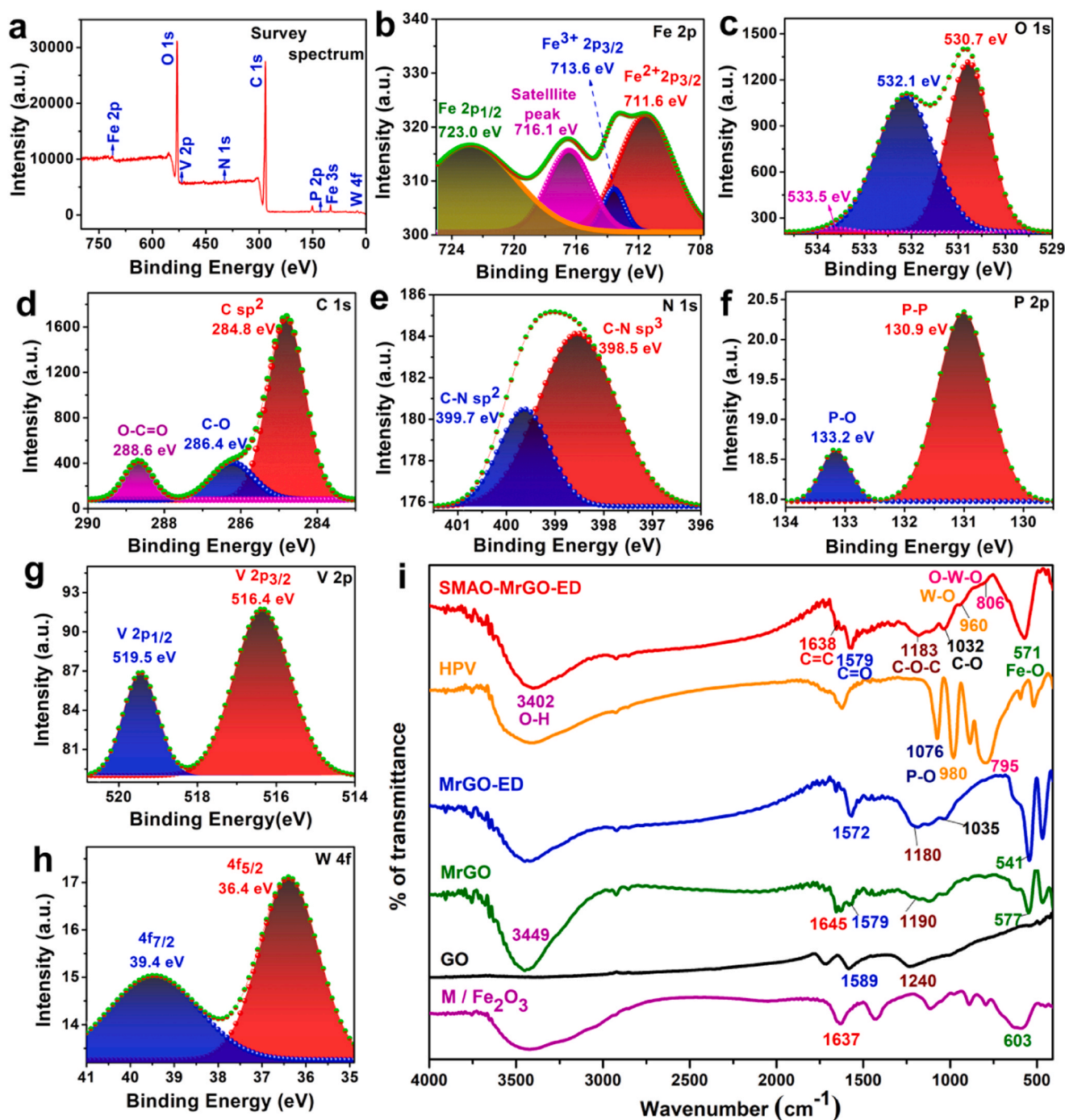


Fig. 5. XPS analysis of SMAO-MrGO-ED, a) Survey spectrum, b) Fe 2p, c) O 1s, d) C 1s, e) N 1s, f) P 2p, g) V 2p, and h) W 4f. i) FT-IR spectra of Fe_2O_3 , GO, MrGO, MrGO-ED, HPV and SMAO-MrGO-ED nanocomposites.

shown in Fig. 5. Here, the Fe 2p peaks (Fig. 5b) locating at 711.6, 713.6, 716.1 and 723.0 eV are corresponding to the Fe 2p_{3/2} (Fe²⁺ and Fe³⁺ peaks), Fe 2p_{3/2} satellite and Fe 2p_{1/2}, respectively [63]. The oxygen elementary XPS spectrum at around 530.7, 532.1 and 533.5 eV should be O1s peaks, which represent the de-convoluted peaks of lattice and chemisorbed oxygen peak (Fig. 5c) [64]. Fig. 5d shows the sp²-C bond in graphene peaks appearing at 284.8 eV, epoxy/hydroxyls groups of C-O position peaks at 286.4 eV and peak at 288.8 eV is due to carboxyl O-C=O binding energy in ED [65]. The N1s spectrum (Fig. 5e) is splitting into two peaks at 398.5 and 399.7 eV, respectively, corresponding to sp³ and sp² C-N bonding [66]. The P 2p spectrum has two fitting peaks of P-P and P-O bondings, as shown in Fig. 5f. One peak at 130.9 eV is assigned to the P-P bonds, while the other peak at 133.2 eV is ascribed to the P-O bonds of heteropoly acid components [67]. Here, the formation of P-P and P-O bonds is mostly attributed to the dissolution of heteropoly acid (HPV) during the synthesis of SMAO-MrGO-ED, while doping of phosphorus (P) has been reported to be a good influence factor to enhance the visible light absorption and induce oxygen vacancies to up-regulate the photocatalytic activity of organic compound degradation [68,69]. Besides, P doped on the surface of semiconductors has proved to enhance the adsorption of O₂, which is significantly important for the formation of reactive oxygen species (ROS) like O₂[•] [70]. In Fig. 5g, V 2p spectrum, the binding energies of V 2p_{3/2} and V 2p_{1/2} are observed at 516.4 and 519.5 eV, respectively corresponding to the vanadium V⁵⁺ in the vanadium substituted heteropoly acid sample [71], so single vanadium atom oxide (SVAO) disperses on the Fe₃O₄ nanoparticles. In Fig. 5h, the two peaks of W 4f_{5/2} and W 4f_{7/2} are present at 36.4 eV and 39.4 eV, respectively. The two peaks are assigned to the heteropoly acid-containing W⁶⁺ oxidation state [3], which confirms that the tungsten atoms on Fe₃O₄ nanoparticles (the HAADF images in Fig. 3) should be single tungsten atom oxide (STAO).

3.5.4. FT-IR Analysis on the adsorption species

FT-IR spectra of Fe₂O₃, GO, MrGO, MrGO-ED, HPV and SMAO-MrGO-ED nanocomposite are shown in Fig. 5i. In the FT-IR spectrum of SMAO-MrGO-ED nanocomposite, the broad band at 3402 cm⁻¹ is associated with the O-H stretching vibration of rGO. The slightly wide peaks at 1638 and 1579 cm⁻¹ are attributed to surface C=C and C=O species in the rGO layer [57]. The broad absorption band at 1183 and 1032 cm⁻¹ correspond to the C-O-C stretching and C-O deformation vibration of phenolic stretching and epoxy symmetrical ring vibrations [71]. For the tungsten vibration peaks indexed to W-O symmetric and anti-symmetric stretching, they appear at 960 cm⁻¹ and 806 cm⁻¹ for SMAO-MrGO-ED, and at 980 cm⁻¹ and 795 cm⁻¹ for H₄[PVW₁₁O₄₀], respectively. The vibrations shift may be due to O-W-O symmetric and antisymmetric deformation vibrations in the two different compounds [67]. Here, the Fe-O bonds appears at ~ 571–577 cm⁻¹ in the Fe₂O₃ and SMAO-MrGO-ED materials [3].

3.6. Photocatalytic activity

3.6.1. The efficiency of the different catalysts

The efficiency of the photodegradation of CF solution (4×10^{-5} M) with different catalysts such as Fe₂O₃, MrGO and SMAO-MrGO-ED nanocomposites are tested as shown in Fig. 6a. The CF removal rates of Fe₂O₃, Fe₃O₄, MrGO-ED and SMAO-MrGO-ED photocatalysts are 47.63%, 71.16%, 77.56% and 88.97% after 90 min irradiation, respectively (Section 2.3). So, the SMAO-MrGO-ED nanocomposites produced the highest photocatalytic degradation activity of CF solution as compared with other catalysts. Meanwhile, the photodegradation efficiency of IBF by various photocatalysts was carried out in Fig. S9a, from which we could find that the IBF decomposition percentages with Fe₂O₃, Fe₃O₄, MrGO-ED and SMAO-MrGO-ED are 44.27%, 56.34%, 64.88% and 83.12% after 120 min light irradiation and SMAO-MrGO-ED presents the highest photoactivity. While kinetic plots (ln (C/C₀)) vs.

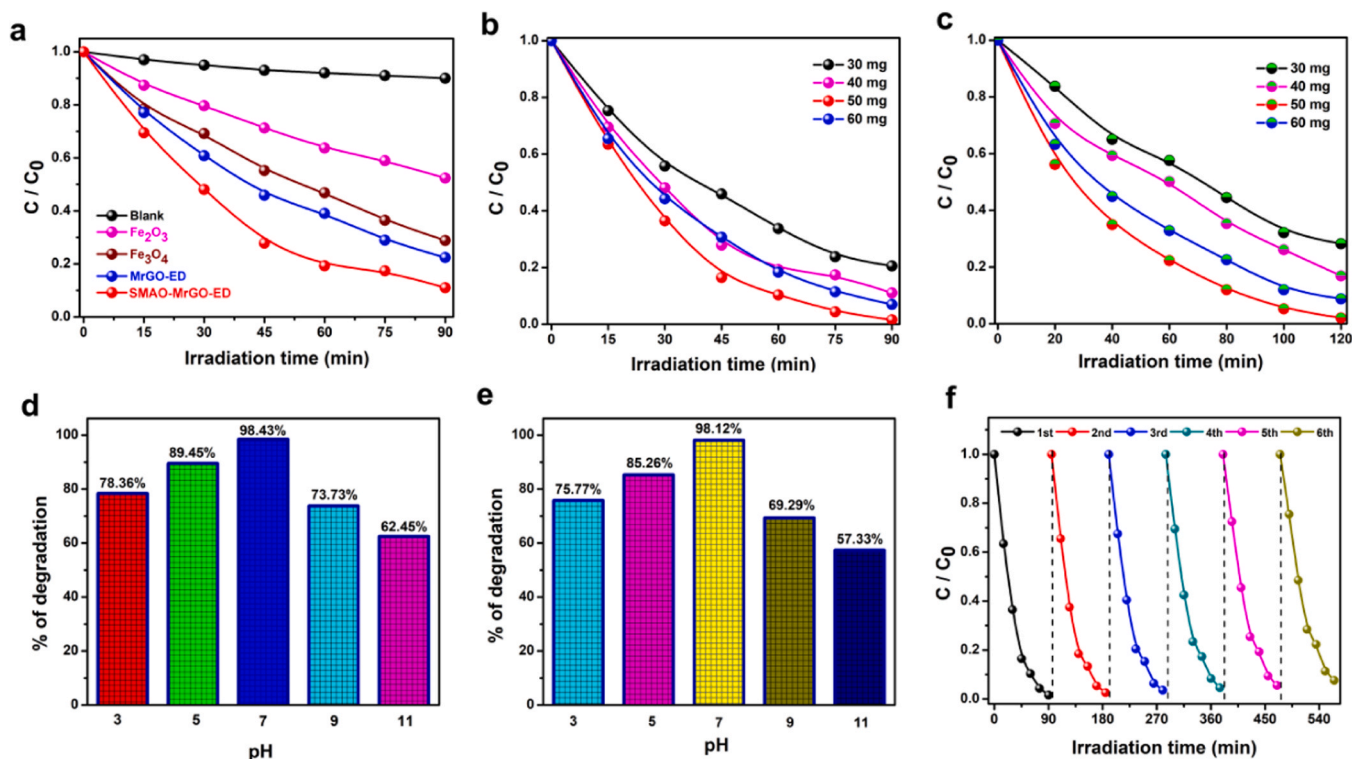


Fig. 6. a) Photodegradation of CF solution by using different catalysts (catalysts: 40 mg, CF conc.: 4×10^{-5} M). Photodegradation of b) CF solution (CF conc.: 4×10^{-5} M) and c) IBF solution (IBF conc.: 2×10^{-4} M) under the variation of SMAO-MrGO-ED catalyst dosage. Effect of solution pH on the degradation efficiency of: d) CF degradation-[CF] = 4×10^{-5} M, e) IBF degradation-[IBF] = 2×10^{-4} M; SMAO-MrGO-ED catalyst suspended = 50 mg/100 mL and irradiation time = 90 min (CF) and 120 min (IBF), respectively. f) Recycle efficiency of the SMAO-MrGO-ED photocatalyst (CF degradation).

irradiation time in Fig. S10a and b) for the photocatalytic degradation of CF and IBF elucidate that SMAO-MrGO-ED takes the highest apparent rate constants k of 0.0454 min^{-1} for CF and 0.0312 min^{-1} for IBF, which is about 6.5, 4.5 and 3.0 times higher than the ones in Fe_2O_3 , Fe_3O_4 and MrGO-ED photocatalysts (Table S3), respectively.

3.6.2. The efficiency of the catalyst dosage

Optimum catalyst dosage is important for the photodegradation of pharmaceutical organic pollutants. To evaluate the optimum condition, catalyst dosage was varied from 30 to 60 mg in CF (Fig. 6b) and IBF (Fig. 6c). Degradation efficiency of CF and IBF increased with the increase of SMAO-MrGO-ED dosage up to 50 mg and then decreased with increasing dosage. The reason for the increase in the efficiency of degradation is the increase in catalyst surface area [67]. But, at higher catalyst loading, such as 60 mg of the photocatalyst, the turbidity of the solution and light scattering by catalyst particles causes the decrease in photodegradation efficiency [3]. So, as concluding above, 50 mg of the SMAO-MrGO-ED photocatalyst is optimum for degradation of CF ($4 \times 10^{-5} \text{ M}$) and IBF ($2 \times 10^{-4} \text{ M}$) solutions. The kinetic parameters of corresponding efficiency in CF and IBF photodegradation with different dosage SMAO-MrGO-ED photocatalyst were estimated in Fig. S10c and d, which concludes that 50 mg of SMAO-MrGO-ED in 100 mL solution has a higher reaction rate as compared to other photocatalyst dosage. Furthermore, to estimate the superior photocatalytic activity of SMAO-MrGO-ED, a comparison of degradation efficiency of CF and IBF with other photocatalysts is shown in Table S4. Here we could find that the current protocol gets higher efficiency catalysts compared with the other photocatalysts data in the literature based on the light source, irradiation time and percentage of degradation efficiency [17,21,22,24,26,72–75].

3.6.3. The effect of pH

The photocatalytic degradation of CF and IBF organic pollutants at different pH (pH from 3 to 11) was studied by using the SMAO-MrGO-ED nanocomposites under visible light irradiation (Fig. 6d and e). The degradation efficiency increases with an increase of pH level up to 7 and then decreases (Fig. 6d). The percentages of CF degradation at pH 3, 5, 7, 9 and 11 are 78.36%, 89.45%, 98.43%, 73.73% and 62.45% respectively for 90 min light irradiation (Fig. 6d). For IBF decomposition, efficiencies are 75.77%, 85.26%, 98.12%, 69.29% and 57.33% at pH 3, 5, 7, 9 and 11 respectively (Fig. 6e). The above results confirm the optimum pH for the degradation of CF and IBF solution is at 7. It should be pointed out that the main reactive photo-oxidizing species by photocatalysis Fe_3O_4 normally should be superoxide radicals ($\text{O}_2^{\bullet-}$) [27]. While in an acidic medium ($\text{pH} < 5$), superoxide radicals ($\text{O}_2^{\bullet-}$) can react with protons forming hydroperoxide radical (HO_2^{\bullet}) [76]. Then, hydroperoxide radicals (HO_2^{\bullet}) have lower oxidant power compared to $\text{O}_2^{\bullet-}$ radicals. And this is the reason for the decrease in activity in the acidic medium (Fig. 6e). However, in the alkaline condition, the OH^- groups in solution may bond with the active sites on Fe_3O_4 , which would lower down the adsorption/diffusion of organic agents and reduce its degradation efficiency [76]. Furthermore, variation of pH in solution may also affect the surface charge of nanoparticles that would not benefit for the dispersibility of nanoparticles. And this is why the neutral solution with SMAO-MrGO-ED photocatalysts could reach a high photo-degradation efficiency (Fig. 6e).

3.6.4. The amplification experiments of SMAO-MrGO-ED catalyst

Fig. S11a and b display an amplified photodegradation experiment of CF and IBF in the presence of 0.5 g and 1.0 g dosage of SMAO-MrGO-ED photocatalyst. As can be seen in Fig. S11, the CF and IBF photodegradation efficiency are 87.55%/96.18% and 90.58%/97.14% for 0.5 g/1.0 g dosage of SMAO-MrGO-ED photocatalyst (for 90 min/120 min light irradiation at $\text{pH} = 7$), respectively. The photodegradation efficiency is enhanced by the increasing dosage from 0.5 g to 1 g, which indicates a possible increasing of active sites on

photocatalysts as enlarging the volume of solution. And this amplification experiment also exhibits a good potential for SMAO-MrGO-ED photocatalyst in industrial application.

3.6.5. Reusability of the photocatalysts

After completion of the degradation reaction, the photocatalyst was recovered by filtration, washed several times with distilled water/ethanol (volume ratio is 1:1) and dried in an air oven for 6 h at 110°C . The dried catalysts were again re-used to degrade the organic pollutants, and the results showed that the SMAO-MrGO-ED nanocomposite has good reusability. However, Fig. 6f shows that the photocatalytic efficiency of the SMAO-MrGO-ED nanocomposites still presents a slightly decrease after the sixth runs recycling (Fig. S12 and Table S5). And such a declension is mostly ascribed to the leaching of catalyst into reaction medium during each recycle [67].

After the photodegradation reaction, the functional groups (C-O, C=O, C=C, C-O-C) and metal oxide peaks on SMAO-MrGO-ED photocatalyst are not changed significantly (Fig. S13). And the morphology of SMAO-MrGO-ED photocatalyst keeps to be the segregated clusters after its reuses (Fig. S14). Furthermore, the chemical state of the elements in SMAO-MrGO-ED presents almost no change after its recycle use for six times (Fig. S15). All the results indicate that SMAO-MrGO-ED photocatalyst has good recycle stability.

3.7. Mechanism of degradation pathways

3.7.1. The bandgap alignment in SMAO-MrGO-ED

As compared to the different photodegradation efficiency of CF and IBF by using Fe_2O_3 , HPV, MrGO-ED and SMAO-MrGO-ED nanocomposites, we can find the SMAO-MrGO-ED has the optimal photoactivity (Fig. 6). Here, the bandgaps of these different compounds were investigated by UV-DRS (Fig. 7a). The band energy of the nanocomposites was estimated by Tauc's plot between $(\alpha\text{Eg})^2$ in Y axis and photon energy in X axis, from which the band gaps of the synthesized Fe_2O_3 , HPV, MrGO-ED and SMAO-MrGO-ED nanocomposites were obtained to be 2.20, 2.93, 2.13 and 2.10 eV, respectively. So, the SMAO-MrGO-ED nanocomposites with a bandgap energy of 2.10 eV confirmed that the catalyst is a visible light active material.

3.7.2. Carrier lifetime in SMAO-MrGO-ED

The photoluminescence (PL) spectra of HPV, Fe_2O_3 , MrGO-ED and SMAO-MrGO-ED nanocomposites were shown in Fig. 7b, which were used to estimate the recombination rate of the photogenerated electron-hole pairs [55]. Compared with other photocatalysts (HPV, Fe_2O_3 , MrGO-ED), lower intensity of SMAO-MrGO-ED nanocomposite indicates reduced electron-hole recombination. Further, lower electron (e^-) – hole (h^+) recombination in SMAO-MrGO-ED may increase the lifetimes of electrons and holes, which results in the increase of photocatalytic efficiency [3].

The photoluminescence decay curves of HPV, Fe_2O_3 , MrGO-ED and SMAO-MrGO-ED nanocomposites were obtained using a 285 nm laser excitation source and the PL decay was recorded at 420 nm (Fig. S16). Lifetimes of HPV, Fe_2O_3 , MrGO-ED and SMAO-MrGO-ED are calculated using the following equation.

$$\tau_{\text{average}} = \sum_{i=1}^3 R_i \tau_i$$

Where R_i is the relative ratio factor which is calculated by

$$R_i = B_i / \left(\sum_{i=1}^3 B_i \right)$$

Table S6 lists the data for HPV, Fe_2O_3 , MrGO-ED and SMAO-MrGO-ED nanocomposites and the average lifetimes are 1.08, 1.27, 1.29 and 1.75 ns, respectively. Here we could find that the lifetime of SMAO-

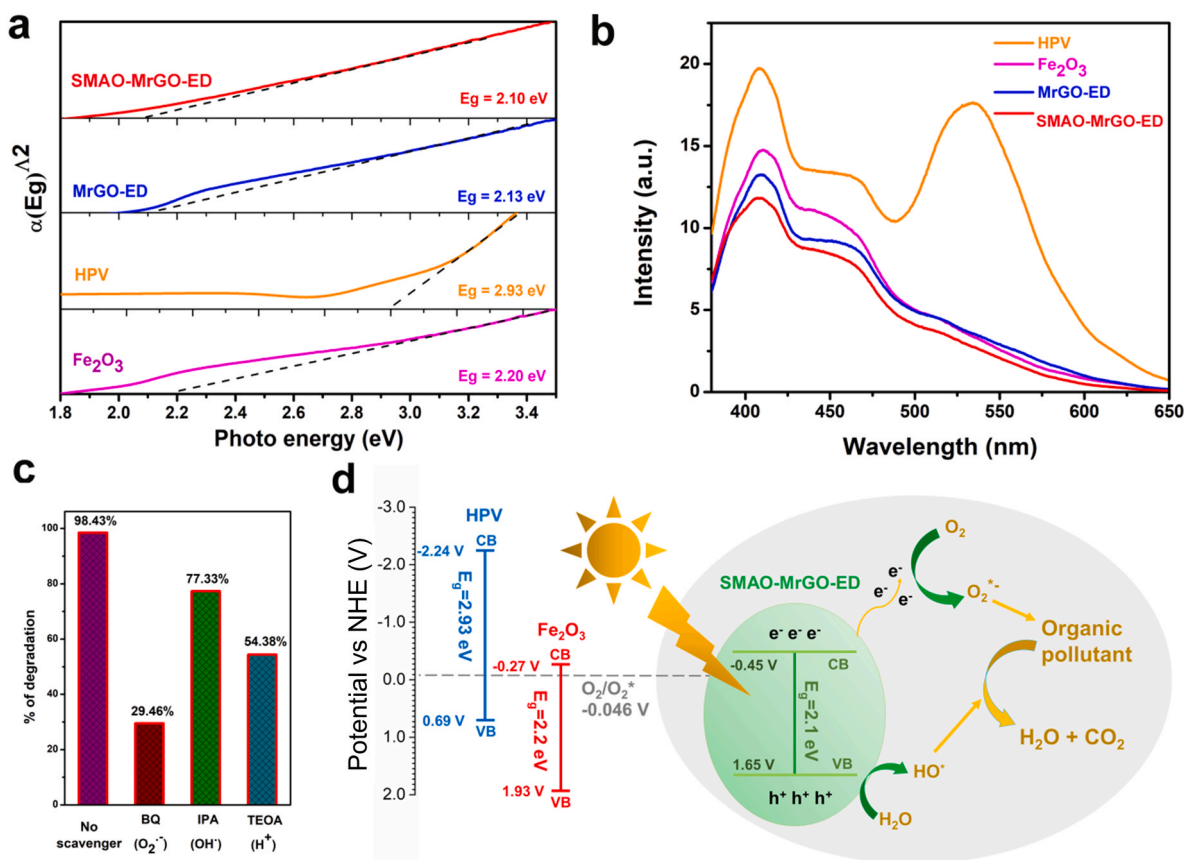


Fig. 7. a) DRS-UV Tauc's plots of Fe_2O_3 , HPV, MrGO-ED and SMAO-MrGO-ED compounds, inset values present the band gap (E_g) of different materials. b) Photoluminescence spectra of HPV, Fe_2O_3 , MrGO-ED and SMAO-MrGO-ED nanocomposites at the excitation wavelength of 370 nm. c) Photodegradation efficiency of CF solution under different scavengers: BQ-0.1 mmol/IPA-0.1 mmol/TEOA-1 mmol (CF conc. 4×10^{-5} M; SMAO-MrGO-ED-50 mg; irradiation time 90 min). d) Schematic illustration of the proposed photocatalytic reaction mechanism of SMAO-MrGO-ED nanocomposite towards the CF and IBF degradation under visible light irradiation.

MrGO-ED photocatalyst materials is higher than that of other nanomaterials. Therefore, SMAO-MrGO-ED should have good photocatalytic activity theoretically.

3.7.3. Oxidation species generation during the photocatalytic degradation

To explain the photocatalytic degradation mechanism of organic pollutants by using SMAO-MrGO-ED nanocomposites, an experiment to find out Reactive Oxidizing Species (ROS) was performed with different scavengers (Fig. 7c). Benzoquinone (BQ), isopropyl alcohol (IPA) and triethanolamine (TEOA) are the scavengers for the superoxide radicals ($O_2^{\bullet-}$), hydroxide radical (OH^{\bullet}) and holes (h^+), respectively (Fig. 7c) [3]. The CF degradation with SMAO-MrGO-ED photocatalyst is highly suppressed by BQ from 98.43% to 29.46% (~69% decrease), which indicates the key role of superoxides radicals in the photocatalytic process. Further, the degradation rate is also slightly decreased with IPA of 77.33% and TEOA of 54.38%. Therefore, the degradation of CF with SMAO-MrGO-ED nanocomposites is mainly dependent on the superoxides radicals ($O_2^{\bullet-}$) produced by the photoreaction of the electron (e^-) and oxygen (O_2). The similar experiment was also carried out for the IBF degradation by using SMAO-MrGO-ED photocatalysts (Fig. S9c), in which the superoxide radicals ($O_2^{\bullet-}$) are still the predominant reaction radicals sustaining the photodegradation of IBF solution.

In addition, electron spin resonance (ESR) spin-trap technique was also applied to confirm the reaction intermediate on the photodegradation of organic agents (Fig. S17). After adding the SMAO-MrGO-ED photocatalysts in DMPO-water solution (in dark, Fig. S17), there is almost no ESR signal for $O_2^{\bullet-}$. When turn on the light source for different times (2–8 min, Fig. S17), the capture of $O_2^{\bullet-}$ by 5,5-dimethyl-

1-pyrroline N-oxide (DMPO) is evidently observed, which confirms that the photogenerated electrons has been generated and stored in rGO to combine with O_2 in water to form the superoxide radicals [77,78]. And the radical of superoxide ($O_2^{\bullet-}$) is the dominated reaction medium to sustain CF/IBF degradation by using SMAO-MrGO-ED photocatalysts.

According to UPS spectra of HPV, Fe_2O_3 and SMAO-MrGO-ED (Fig. S18), we calculated the conduction band (CB) and valence band (VB) values of HPV as -2.26 V and -5.19 V, Fe_2O_3 as -4.23 V and -6.43 V, and SMAO-MrGO-ED as -4.05 V and -6.15 V, respectively. Using the standard hydrogen electrode (SHE) as a reference, the CB and VB edges of SMAO-MrGO-ED are -0.45 V and 1.65 V, HPV are -2.24 V and 0.69 V, and Fe_2O_3 are -0.27 V and 1.93 V, respectively. Based on the above calculations, a degradation mechanism is proposed in Fig. 7d, in which the electrons transfer from the conduction band of SMAO-MrGO-ED to rGO electron transfer layer for the separation electron-hole [71]. Furthermore, reduced graphene oxide traps the photogenerated electron and gives oxygen to form superoxide $O_2^{\bullet-}$ radicals [71], which may further reduce the recombination of photo-excited electron-hole pairs. This agreed well with the experimental report in the reactive oxidizing species methods that $O_2^{\bullet-}$ radicals play key role on the photodegradation of CF (Fig. 7c).

In addition, the absorption capacity of organic molecules on Fe_3O_4 nanoparticles is more efficient than Fe_2O_3 [20], rGO, C_3N_4 and other catalysts [79]. Zhu et al. reported the comparison of absorption curves of tetracycline molecules on the different samples, and Fe_3O_4 /g- C_3N_4 nanocomposite has highest adsorption capacity than g- C_3N_4 and Ag/ Fe_3O_4 /g- C_3N_4 . While, the main contact between Fe_3O_4 and organic molecules may be due to the electrical stabilization of Fe_3O_4

nanoparticles to organic pollutants under the action of gravity [79]. Further Fe_3O_4 material produce photogenerated electrons efficiently due to its good electron-hole pairs separation ability. Therefore, Fe_3O_4 nanoparticles can efficiently adsorb pollutants and export electrons to the reaction medium [79].

Furthermore, the effect of single-atom photocatalytic system consists of three main components, (i) high number density of active catalytic sites. From the previous HAADF images, EDS and ICP results of SMAO-MrGO-ED, we have observed a large number of single atoms covered on the Fe_3O_4 nanoparticles, which may offer the active sites for photocatalysis. (ii) light-harvesting property [80]. In SMAO-MrGO-ED photocatalyst, the STAO/SVAO play the key roles due to the higher density of active sites and the light-harvesting units [36]. Time-resolved photoluminescence decay curves of different catalysts (Fig. S16) reveal that SMAO-MrGO-ED is efficient for light harvesting and charge separation and transfer. (iii) The electron transfer medium. The intervalence charge transfer of electron from V and W single atom oxides to reaction species has been disclosed [81], in which the electrons are stored and provided on the STAO or SVAO to benefit the formation of reactive oxidation species (ROS). In addition, Wang et al. [36] also reported the inter-d band electron transfer is different between STAO and WO_3 crystal. Higher density of active site from STAO and the electron transfer of inter-d orbital on an excited state from quasi-atom mechanisms play a key role on the higher efficiency of single atom photocatalysts [36]. Finally, the photogenerated electrons excite O_2 molecules to form $\text{O}_2^{\bullet-}$ radicals, which bombarded the organic pollutants to produce the CO_2 and H_2O main products. Therefore, the single atoms of W/V metal oxides have a potential impact on photocatalytic reaction steps, light-harvesting, charge separation and transfer, and surface catalytic reaction.

3.7.4. The charge transport mechanism of SMAO-MrGO-ED nanocomposites

As compared the crystal structure (Figs. 1 and S2) and morphology (Figs. 2 and S3) between SMAO-MrGO-ED and $\text{Fe}_3\text{O}_4/\text{rGO}/\text{ED}/\text{HPV}$ nanocomposites, though the main phase of these two catalysts are Fe_3O_4 , but HPV on Fe_3O_4 nanoparticles has been dissolved completely on SMAO-MrGO-ED to form STAO/SVAO. In order to check the influence of STAO/SVAO on interfacial charge transport, the transient photocurrent responses were recorded for five intermittent light on-off cycles in Fig. S19a. As turning on the light illumination, the transient photocurrent density of SMAO-MrGO-ED nanocomposites is larger than the one in $\text{Fe}_3\text{O}_4/\text{rGO}/\text{ED}/\text{HPV}$ counterpart, and a larger current density implies a superior potential to migrate photogenerated electrons and holes [82]. While, for the Nyquist plots of Electrochemical Impedance Spectroscopy (EIS) in Fig. S19b, very low solution resistance (R_s) values of $0.66\ \Omega$ was noticed for SMAO-MrGO-ED as compared with the one of $0.85\ \Omega$ in $\text{Fe}_3\text{O}_4/\text{rGO}/\text{ED}/\text{HPV}$. And the charge transfer resistance (R_{ct}) value of the SMAO-MrGO-ED was $450.3\ \Omega$, which was much lower than the one of $580.6\ \Omega$ in $\text{Fe}_3\text{O}_4/\text{rGO}/\text{ED}/\text{HPV}$. In addition, the linear sweep voltammetry (LSV) tests of prepared SMAO-MrGO-ED and $\text{Fe}_3\text{O}_4/\text{rGO}/\text{ED}/\text{HPV}$ were also investigated as shown in Fig. S19c and d, a negative shift of oxygen and a positive shift of hydrogen evolution potentials in SMAO-MrGO-ED are mostly induced by a rapid charge separation and formation of more active sites for catalytic oxidation [83, 84]. All these results elucidate that SMAO-MrGO-ED presents a faster charge transfer and low charge transport resistance from electrocatalysts into solution, that would be beneficial for enhancing the photocatalytic performance.

3.7.5. The catalysts adsorption studies

The dark adsorption experiment of different catalysts was performed with aqueous solutions of CF and IBF in Fig. S20 and Table S7. In the absence of light irradiation, the adsorption process takes place on the catalysts' surface as seen in Fig. S20. And adsorption percentage of CF and IBF increases for all catalysts till the equilibrium at about 30 min

(Fig. S20a and b). However, the highest adsorption of CF (28.39%) and IBF (24.35%) was observed in SMAO-MrGO-ED photocatalyst as compared with other catalysts of Fe_2O_3 , Fe_3O_4 and MrGO-ED (Fig. S20a and b), which also corresponded to the highest molecules adsorption kinetics (Fig. S20c, d and Table S7). Though the adsorption of CF and IBF molecules on SMAO-MrGO-ED is good, the reusability of this catalyst shows almost no significant loss in efficiency (Figs. 6f and S9b) due to a good maintain of catalyst's structure and morphology even after six cycles using (Figs. S13–S15). All these results confirm that the surface of SMAO-MrGO-ED keeps high efficiency for adsorption and photodegradation of antibiotic organics.

3.7.6. Identification of photocatalytic degradation intermediates

In order to understand the by-products during photocatalytic reaction, the intermediates appeared at the reaction of first 60 min of CF photodegradation were estimated by Gas chromatography-Mass spectroscopy (GC-MS). Ten different retention times with higher intensity are selected in the GC-MS and the corresponding ten intermediate compounds are detected by mass spectrum (Fig. 8 and Table S8). Some of the intermediates were not detected due to their quick oxidation into derivatives (t_R : 18.988 min, following data in Table S8). The degradation process of CF is firstly converted into quinolone moiety (m/z 405), followed by the bond breaking of piperazine ring (m/z 355), and then further converted to eight intermediate products (m/z : 336, 308, 296, 280, 270, 252, 224, 209) in a sequence within 60 min (Fig. 8). Finally, the intermediates are converted to low-molecular organic and CO_2 , H_2O and mineral acid. Therefore, the by-product generation during the photodegradation of CF organic pollutant in the presence of SMAO-MrGO-ED nanocomposites successfully evaluated. While, for the photodegradation pathway of IBF using SMAO-MrGO-ED photocatalysts, it should be very similar with the ones in a titania photodegradation process [85], and the reaction conditions such as aqueous solution, pH value range (pH 7), temperature as well as the important active species of $\text{O}_2^{\bullet-}$ are almost the same with this work. As shown in this report, superoxide radicals initially trigger the degradation of IBF compound to form a higher molecular intermediate namely side chain products. And then, intermediates decompose into subsequent deep oxidation products, ring opening, and finally the final products of CO_2 and H_2O are mineralized. From this point of view, the degradation pathway of IBF is very similar with the one in CF decomposition in Fig. 7d.

4. Conclusion

Sandwich-like photocatalyst SMAO-MrGO-ED nanocomposites were successfully synthesized by hydrothermal method and characterized using XRD, HR-SEM, HAADF STEM, EDX, UV-DRS and FT-IR analysis. The XRD, HR-SEM, HAADF-STEM, EXAFS and XANES analyses confirm the formation of Fe_3O_4 nanomaterials with the adsorption of single tungsten/vanadium atom oxide (ST/VAO) on the nanoparticles' surface. The rGO-ED and HPV materials are required for the complete conversion of Fe_2O_3 into Fe_3O_4 . Meanwhile, SMAO-MrGO-ED is found to have highly efficient visible light photodegradation of ciprofloxacin and ibuprofen. The optimized catalyst dosage is 50 mg of the SMAO-MrGO-ED photocatalyst for CF ($4 \times 10^{-5}\ \text{M}$) and IBF ($2 \times 10^{-4}\ \text{M}$) solution under visible radiation. Superoxide radicals are found to mainly involve in the degradation of CF and IBF solutions, which induced the SMAO-MrGO-ED to perform the superior photocatalytic activity and chemical stability as confirmed by the reusability test.

Credit authorship contribution statement

Karuppaiah Selvakumar: Conceptualization, Formal analysis, Investigation, Writing – review & editing. **Yueshuai Wang:** Investigation, Formal analysis, Writing – review & editing, Software. **Yue Lu:** Conceptualization, Writing – review & editing. **Bohai Tian:** Investigation, Formal analysis, Data curation. **Zeyu Zhang:** Investigation, Formal

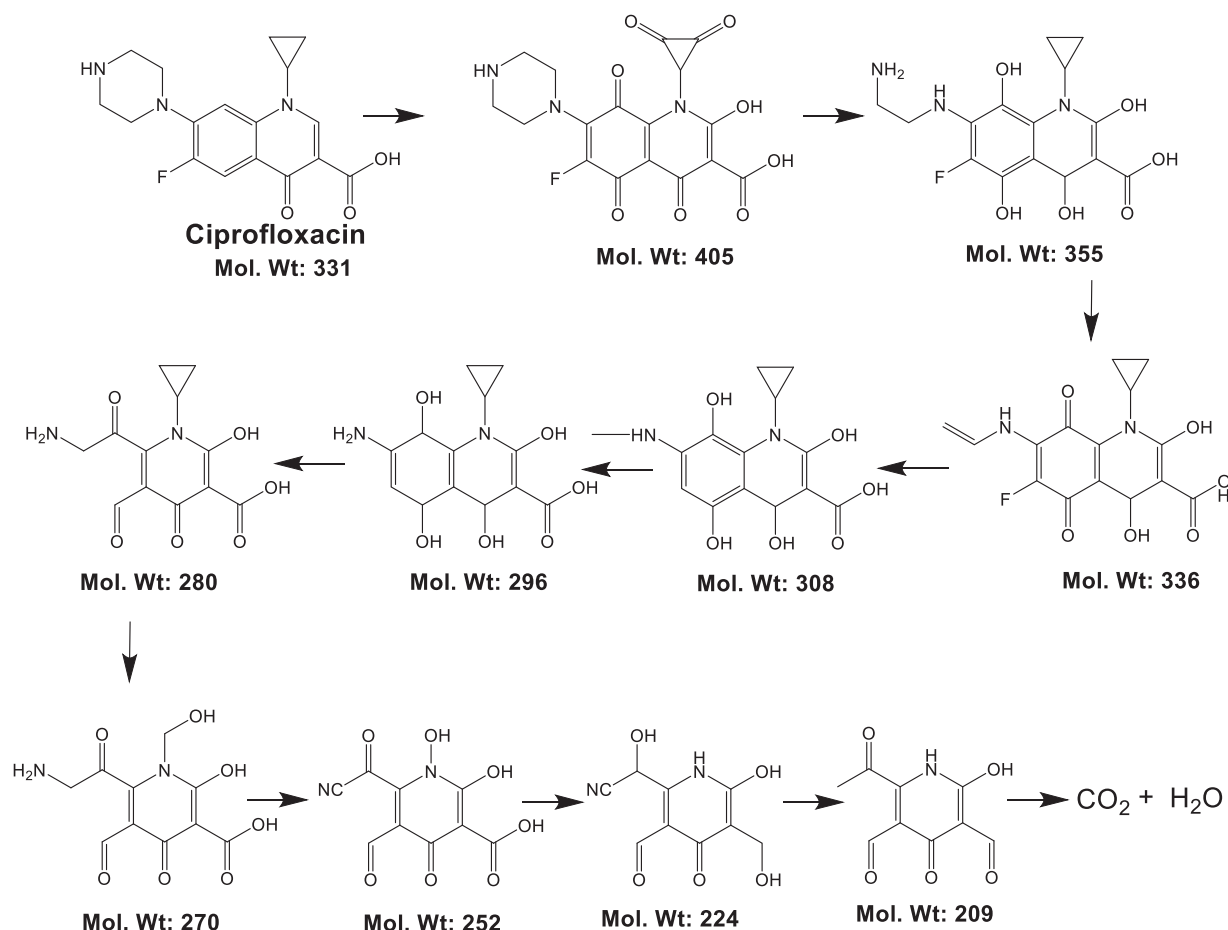


Fig. 8. Proposed photodegradation pathway of ciprofloxacin compound using SMAO-MrGO-ED photocatalyst.

analysis. **Jingcong Hu**: Formal analysis, Data curation. **Annamalai Raja**: Investigation. **Muthuraj Arunpandian**: Formal analysis. **Mee-nakshisundaram Swaminathan**: Conceptualization, Formal analysis, Writing – review & editing. **Hongxing Dai**: Formal analysis, Writing – review & editing. **Manling Sui**: Conceptualization, Writing – review & editing, Formal analysis.

Declaration of Competing Interest

The authors declare that they have no known competing financial interests or personal relationships that could have appeared to influence the work reported in this paper.

Acknowledgments

Karuppiah Selvakumar and Yueshuai Wang are equal contribution. Thanks to Jiangshan Qu and Rengui Li from Dalian Institute of Chemical Physics, Chinese Academy of Sciences for their support of ESR tests. And thanks to Lirong Zheng from the Institute of High Energy Physics, Chinese Academy of Sciences for supporting the EXAFS experiments. Thanks to Kalasalingam Academy of research and Education for preparation and initial characterization of catalysts. This work was supported by the National Key Research and Development Program of China (2016YFB0700700), the National Natural Science Foundation of China (11704015, 51621003, 12074016), the Scientific Research Key Program of Beijing Municipal Commission of Education, China (KZ201310005002), the General Program of Science and Technology Development Project of Beijing Municipal Education Commission (KM202110005003) and the Beijing Innovation Team Building Program, China (IDHT20190503).

Appendix A. Supplementary material

Supplementary data associated with this article can be found in the online version at [doi:10.1016/j.apcatb.2021.120740](https://doi.org/10.1016/j.apcatb.2021.120740).

References

- [1] N.H. Tran, M. Reinhard, K.Y. Gin, Occurrence and fate of emerging contaminants in municipal wastewater treatment plants from different geographical regions-a review, *Water Res.* 133 (2018) 182–207, <https://doi.org/10.1016/j.watres.2017.12.029>.
- [2] Y. Wang, Y. Li, A. Hu, A. Rashid, M. Ashfaq, Y. Wang, H. Wang, H. Luo, C. Yu, Q. Sun, Monitoring, mass balance and fate of pharmaceuticals and personal care products in seven wastewater treatment plants in Xiamen City, China, *J. Hazard. Mater.* 354 (2018) 81–90, <https://doi.org/10.1016/j.jhazmat.2018.04.064>.
- [3] K. Selvakumar, A. Raja, M. Arunpandian, K. Stalindurai, P. Rajasekaran, P. Sami, E. R. Nagarajan, M. Swaminathan, Efficient photocatalytic degradation of ciprofloxacin and bisphenol A under visible light using Gd₂WO₆ loaded ZnO/bentonite nanocomposite, *Appl. Surf. Sci.* 481 (2019) 1109–1119, <https://doi.org/10.1016/j.apsusc.2019.03.178>.
- [4] A.M. Ali, H.T. Ronning, L.K. Sydnese, W.M. Alarif, R. Kallenborn, S.S. Al-Lihaibi, Detection of PPCPs in marine organisms from contaminated coastal waters of the Saudi Red Sea, *Sci. Total Environ.* 621 (2018) 654–662, <https://doi.org/10.1016/j.scitotenv.2017.11.298>.
- [5] Z.-H. Diao, X.-R. Xu, D. Jiang, G. Li, J.-J. Liu, L.-J. Kong, L.-Z. Zuo, Enhanced catalytic degradation of ciprofloxacin with FeS₂/SiO₂ microspheres as heterogeneous Fenton catalyst: kinetics, reaction pathways and mechanism, *J. Hazard. Mater.* 327 (2017) 108–115, <https://doi.org/10.1016/j.jhazmat.2016.12.045>.
- [6] A. Hassani, A. Khataee, S. Karaca, M. Fathinia, Heterogeneous photocatalytic ozonation of ciprofloxacin using synthesized titanium dioxide nanoparticles on a montmorillonite support: parametric studies, mechanistic analysis and intermediates identification, *RSC Adv.* 6 (2016) 87569–87583, <https://doi.org/10.1039/C6RA19191F>.
- [7] B.D. Witte, J. Dewulf, K. Demeestere, H.V. Langenhove, Ozonation and advanced oxidation by the peroxone process of ciprofloxacin in water, *J. Hazard. Mater.* 161 (2009) 701–708, <https://doi.org/10.1016/j.jhazmat.2008.04.021>.

- [8] E.M. Golet, A.C. Alder, W. Giger, Environmental exposure and risk assessment of fluoroquinolone antibacterial agents in wastewater and river water of the Glatt valley watershed, Switzerland, *Environ. Sci. Technol.* 36 (2002) 3645–3651, <https://doi.org/10.1021/es0256212>.
- [9] A. Hartmann, E.M. Golet, S. Gartiser, A.C. Alder, T. Koller, R.M. Widmer, Primary DNA damage but not mutagenicity correlates with ciprofloxacin concentrations in German hospital wastewaters, *Arch. Environ. Contam. Toxicol.* 36 (1999) 115–119, <https://doi.org/10.1007/s002449900449>.
- [10] S.E. Jorgensen, B. Halling-Sorensen, Drugs in the environment, *Chemosphere* 40 (2000) 691–699, [https://doi.org/10.1016/S0045-6535\(99\)00438-5](https://doi.org/10.1016/S0045-6535(99)00438-5).
- [11] M.D. Adjei, T.M. Heinze, J. Deck, J.P. Freeman, A.J. Williams, J.B. Sutherland, Transformation of the antibacterial agent norfloxacin by environmental mycobacteria, *Appl. Environ. Microbiol.* 72 (2006) 5790–5793, <https://doi.org/10.1128/AEM.03032-05>.
- [12] Y. Gu, J. Yperman, R. Carleer, J. Dhaen, J. Maggen, S. Vanderheyden, K. Vanreppelen, R. Machado Garcia, Adsorption and photocatalytic removal of Ibuprofen by activated carbon impregnated with TiO₂ by UV-Vis monitoring, *Chemosphere* 217 (2019) 724–731, <https://doi.org/10.1016/j.chemosphere.2018.11.068>.
- [13] J. Wang, B. He, D. Yan, X. Hu, Implementing ecopharmacovigilance (EPV) from a pharmacy perspective: a focus on non-steroidal anti-inflammatory drugs, *Sci. Total Environ.* 603–604 (2017) 772–784, <https://doi.org/10.1016/j.scitotenv.2017.02.209>.
- [14] A. Bialk-Bielinska, J. Kumirska, M. Borecka, M. Caban, M. Paszkiewicz, K. Pazdro, P. Stepnowski, Selected analytical challenges in the determination of pharmaceuticals in drinking/marine waters and soil/sediment samples, *J. Pharm. Biomed. Anal.* 121 (2016) 271–296, <https://doi.org/10.1016/j.jpba.2016.01.016>.
- [15] C. Aristizabal-Ciro, A.M. Botero-Coy, F.J. Lopez, G.A. Penuela, Monitoring pharmaceuticals and personal care products in reservoir water used for drinking water supply, *Environ. Sci. Pollut. Res.* 24 (2017) 7335–7347, <https://doi.org/10.1007/s11356-016-8253-1>.
- [16] A. Raja, P. Rajasekaran, K. Selvakumar, M. Arunpandian, S. Asath Bahadur, M. Swaminathan, Wool roving textured reduced graphene oxide-HoVO₄-ZnO nanocomposite for photocatalytic and supercapacitor performance, *Electrochim. Acta* 328 (2019), 135062, <https://doi.org/10.1016/j.electacta.2019.135062>.
- [17] A. Salma, S. Thoroe-Boveleth, T.C. Schmidt, J. Tuerk, Dependence of transformation product formation on pH during photolytic and photocatalytic degradation of ciprofloxacin, *J. Hazard. Mater.* 313 (2016) 49–59, <https://doi.org/10.1016/j.jhazmat.2016.03.010>.
- [18] O. Akhavan, Graphene nanomesh by ZnO nanorod photocatalysts, *ACS Nano* 4 (2010) 4174–4180, <https://doi.org/10.1021/nn1007429>.
- [19] A. Kusior, K. Michalec, P. Jelen, M. Radecka, Shaped Fe₂O₃ nanoparticles-synthesis and enhanced photocatalytic degradation towards RhB, *Appl. Surf. Sci.* 476 (2019) 342–352, <https://doi.org/10.1016/j.apsusc.2018.12.113>.
- [20] L. Ren, W. Zhou, B. Sun, H. Li, P. Qiao, Y. Xu, J. Wu, K. Lin, H. Fu, Defects-engineering of magnetic γ -Fe₂O₃ ultrathin nanosheets/mesoporous black TiO₂ hollow sphere heterojunctions for efficient charge separation and the solar-driven photocatalytic mechanism of tetracycline degradation, *Appl. Catal. B Environ.* 240 (2019) 319–328, <https://doi.org/10.1016/j.apcatb.2018.08.033>.
- [21] X. Lu, Y. Wang, X. Zhang, G. Xu, D. Wang, J. Lv, Z. Zheng, Y. Wu, NiS and MoS₂ nanosheet co-modified graphitic C₃N₄ ternary heterostructure for high efficient visible light photodegradation of antibiotic, *J. Hazard. Mater.* 341 (2018) 10–19, <https://doi.org/10.1016/j.jhazmat.2017.07.004>.
- [22] Y. Deng, L. Tang, C. Feng, G. Zeng, J. Wang, Y. Zhou, Y. Liu, B. Peng, H. Feng, Construction of plasmonic Ag modified phosphorous-doped ultrathin g-C₃N₄ nanosheets/BiVO₄ photocatalyst with enhanced visible-near-infrared response ability for ciprofloxacin degradation, *J. Hazard. Mater.* 344 (2018) 758–769, <https://doi.org/10.1016/j.jhazmat.2017.11.027>.
- [23] R. Hassandoost, S. Rahim Pouran, A. Khataee, Y. Orooji, S. Woo Joo, Hierarchically structured ternary heterojunctions based on Ce³⁺/Ce⁴⁺ modified Fe₃O₄ nanoparticles anchored onto graphene oxide sheets as magnetic visible-light-active photocatalysts for decontamination of oxytetracycline, *J. Hazard. Mater.* 376 (2019) 200–211, <https://doi.org/10.1016/j.jhazmat.2019.05.035>.
- [24] Y. Li, Y. Fu, M. Zhu, Green synthesis of 3D tripyramid TiO₂ architectures with assistance of aloe extracts for highly efficient photocatalytic degradation of antibiotic ciprofloxacin, *Appl. Catal. B Environ.* 260 (2020) 118149, <https://doi.org/10.1016/j.apcatb.2019.118149>.
- [25] N.D. Banic, B.F. Abramovic, J.B. Krstic, D.V. Sojic Merkulova, N.L. Fincur, M. N. Mitric, Novel WO₃/Fe₃O₄ magnetic photocatalysts: preparation, characterization and thiaclopid photodegradation, *J. Ind. Eng. Chem.* 70 (2019) 264–275, <https://doi.org/10.1016/j.jiec.2018.10.025>.
- [26] F. Wang, X. Yu, M. Ge, S. Wu, One-step synthesis of TiO₂/ γ -Fe₂O₃/GO nanocomposites for visible light-driven degradation of Ciprofloxacin, *Chem. Eng. J.* 384 (2020) 123381, <https://doi.org/10.1016/j.cej.2019.123381>.
- [27] M. Mousavi, A. Habibi-Yangjeh, Magnetically separable ternary g-C₃N₄/Fe₃O₄/BiOI nanocomposites: novel visible-light-driven photocatalysts based on graphitic carbon nitride, *J. Colloid Interface Sci.* 465 (2016) 83–92, <https://doi.org/10.1016/j.jcis.2015.11.057>.
- [28] D. Bektova, M. Motola, H. Sopha, J. Michalicka, V. Cismancova, F. Dvorak, L. Hromadko, B. Frumarova, M. Stoica, J.M. Macak, One-step decoration of TiO₂ nanotubes with Fe₃O₄ nanoparticles: synthesis, and photocatalytic, and magnetic properties, *ACS Appl. Nano Mater.* 3 (2) (2020) 1553–1563, <https://doi.org/10.1021/acsnm.9b02337>.
- [29] D. Xu, W. Shi, C. Song, M. Chen, S. Yang, W. Fan, B. Chen, In-situ synthesis and enhanced photocatalytic activity of visible-light-driven plasmonic Ag/AgCl/NaTaO₃ nanocubes photocatalysts, *Appl. Catal. B: Environ.* 191 (2016) 228–234, <https://doi.org/10.1016/j.apcatb.2016.03.036>.
- [30] S. Liu, Q. Hu, J. Qiu, F. Wang, W. Lin, F. Zhu, C. Wei, N. Zhou, G. Ouyang, Enhanced photocatalytic degradation of environmental pollutants under visible irradiation by a composite coating, *Environ. Sci. Technol.* 51 (2017) 5137–5145, <https://doi.org/10.1021/acs.est.7b00350>.
- [31] X. Qian, M. Ren, Y. Zhu, D. Yue, Y. Han, J. Jia, Y. Zhao, Visible light assisted heterogeneous Fenton-like degradation of organic pollutant via α -FeOOH/mesoporous carbon composites, *Environ. Sci. Technol.* 51 (2017) 3993–4000, <https://doi.org/10.1021/acs.est.6b06429>.
- [32] M. Jahan, Q. Bao, J.X. Yang, K.P. Loh, Structure-directing role of graphene in the synthesis of metal-organic framework nanowire, *J. Am. Chem. Soc.* 132 (2010) 14487–14495, <https://doi.org/10.1021/ja105089w>.
- [33] L. Tang, C.T. Jia, Y.C. Xue, L. Li, A.Q. Wang, G. Xu, N. Liu, M.H. Wu, Fabrication of compressible and recyclable macroscopic g-C₃N₄/GO aerogel hybrids for visible-light harvesting: a promising strategy for water remediation, *Appl. Catal. B: Environ.* 219 (2017) 241–248, <https://doi.org/10.1016/j.apcatb.2017.07.053>.
- [34] B. Liu, Z.T. Yu, J. Yang, H. Wu, Y.Y. Liu, J.F. Ma, First three-dimensional inorganic-organic hybrid material constructed from an “inverted Keggin” polyoxometalate and a copper (I)-organic complex, *Inorg. Chem.* 50 (2011) 8967–8972, <https://doi.org/10.1021/ic201135g>.
- [35] W. Chen, J. Pei, C.-T. He, J. Wan, H. Ren, Y. Wang, J. Dong, K. Wu, W.-C. Cheong, J. Mao, X. Zheng, W. Yan, Z. Zhuang, C. Chen, Q. Peng, D. Wang, Y. Li, Single tungsten atoms supported on MOF-derived N-doped carbon for robust electrochemical hydrogen evolution, *Adv. Mater.* 30 (2018) 1800396, <https://doi.org/10.1002/adma.201800396>.
- [36] C. Wang, A. Li, C. Li, S. Zhang, H. Li, X. Zhou, L. Hu, Y. Feng, K. Wang, Z. Zhu, R. Shao, Y. Chen, P. Gao, S. Mao, J. Huang, Z. Zhang, X. Han, Ultrahigh photocatalytic rate at a single-metal-atom-oxide, *Adv. Mater.* 31 (2019) 1903491, <https://doi.org/10.1002/adma.201903491>.
- [37] R. Lang, W. Xi, J.-C. Liu, Y.-T. Cui, T. Li, A.F. Lee, F. Chen, Y. Chen, L. Li, L. Li, J. Lin, S. Miao, X. Liu, A.-Q. Wang, X. Wang, J. Luo, B. Qiao, J. Li, T. Zhang, Non defect-stabilized thermally stable single-atom catalyst, *Nat. Commun.* 10 (2019) 234, <https://doi.org/10.1038/s41467-018-08136-3>.
- [38] J. Yan, L. Kong, Y. Ji, J. White, Y. Li, J. Zhang, P. An, S. Liu, S.-T. Lee, T. Ma, Single atom tungsten doped ultrathin α -Ni(OH)₂ for enhanced electrocatalytic water oxidation, *Nat. Commun.* 10 (2019) 2149, <https://doi.org/10.1038/s41467-019-09845-z>.
- [39] H. Fakhri, A.-R. Mahjoub, H. Aghayan, Effective removal of methylene blue and cerium by a novel pair set of heteropoly acids based functionalized graphene oxide: adsorption and photocatalytic study, *Chem. Eng. Res. Des.* 120 (2017) 303–315, <https://doi.org/10.1016/j.chemd.2017.02.030>.
- [40] K. Selvakumar, T. Shanmugaprabha, R. Annappoorani, P. Sami, One-pot three-component synthesis of bis(indolyl)methanes under solvent-free condition using heteropoly-11-tungsto-1-vanadophosphoric acid supported on natural clay as catalyst, *Synth. Commun.* 47 (2017) 913–927, <https://doi.org/10.1080/00397911.2017.1296159>.
- [41] J. Zielinski, I. Zglinicka, L. Znak, Z. Kaszkur, Reduction of Fe₂O₃ with hydrogen, *Appl. Catal. A* 381 (2010) 191–196, <https://doi.org/10.1016/j.apcata.2010.04.003>.
- [42] F. Cardenas-Lizana, S. Gomez-Quero, N. Perret, M.A. Keane, Gold catalysis at the gas-solid interface: role of the support in determining activity and selectivity in the hydrogenation of *m*-dinitrobenzene, *Catal. Sci. Technol.* 1 (2011) 652–661, <https://doi.org/10.1039/C1CY00051A>.
- [43] D. Long, E. Burkholder, L. Cronin, Polyoxometalate clusters, nanostructures and materials: from self assembly to designer materials and devices, *Chem. Soc. Rev.* 36 (2007) 105–121, <https://doi.org/10.1039/B502666K>.
- [44] Y. Guo, C. Hu, Heterogeneous photocatalysis by solid polyoxometalates, *J. Mol. Catal. A: Chem.* 262 (2007) 136–148, <https://doi.org/10.1016/j.molcata.2006.08.039>.
- [45] E. Gkika, A. Troupis, A. Hiskia, E. Papaconstantinou, Photocatalytic reduction of chromium and oxidation of organics by polyoxometalates, *Appl. Catal. B: Environ.* 62 (2006) 28–34, <https://doi.org/10.1016/j.apcatb.2005.06.012>.
- [46] B. Wen, X.X. Wang, W.Q. Cao, H.L. Shi, M.M. Lu, G. Wang, H.B. Jin, W.Z. Wang, J. Yuan, M.S. Cao, Reduced graphene oxides: the thinnest and most light weight materials with highly efficient microwave attenuation performances of the carbon world, *Nanoscale* 6 (11) (2014) 5754–5761, <https://doi.org/10.1039/C3NR06717C>.
- [47] M. Masteri-Farahania, J. Movassagh, F. Taghavi, P. Eghbali, F. Salimi, Magnetite-polyoxometalate hybrid nanomaterials: synthesis and characterization, *Chem. Eng. J.* 184 (2012) 342–346, <https://doi.org/10.1016/j.cej.2011.12.094>.
- [48] E. Rafiee, S. Eavani, H₃PW₁₂O₄₀ supported on silica-encapsulated γ -Fe₂O₃ nanoparticles: a novel magnetically-recoverable catalyst for three-component Mannich-type reactions in water, *Green Chem.* 13 (2011) 2116–2122, <https://doi.org/10.1039/C1GC15291B>.
- [49] T. Cheng, D. Zhang, H. Li, G. Liu, Magnetically recoverable nanoparticles as efficient catalysts for organic transformations in aqueous medium, *Green Chem.* 16 (7) (2014) 3401–3427, <https://doi.org/10.1039/C4GC00458B>.
- [50] Y. Zhu, L.P. Stubbs, F. Ho, R. Liu, C.P. Ship, J.A. Maguire, N.S. Hosmane, Magnetic nanocomposites: a new perspective in catalysis, *Chem. Cat. Chem.* 2 (2010) 365–374, <https://doi.org/10.1002/cctc.200900314>.
- [51] J. Mondal, T. Sen, A. Bhaumik, Fe₃O₄@mesoporous SBA-15: a robust and magnetically recoverable catalyst for one-pot synthesis of 3,4-dihydropyrimidin-2 (1H)-ones via the Biginelli reaction, *Dalton Trans.* 41 (2012) 6173–6181, <https://doi.org/10.1039/C2DT30106G>.

- [52] R. Tayebee, M.M. Amini, H. Rostamian, A. Aliakbari, Preparation and characterization of a novel Wells–Dawson heteropolyacid-based magnetic inorganic–organic nanohybrid catalyst $\text{H}_6\text{P}_2\text{W}_{18}\text{O}_{62}/\text{pyridino-Fe}_3\text{O}_4$ for the efficient synthesis of 1-amidoalkyl-2-naphthols under solvent-free conditions, *Dalton Trans.* 43 (2014) 1550–1563, <https://doi.org/10.1039/C3DT51594J>.
- [53] Zillillah, T.A. Ngu, Z. Li, Phosphotungstic acid-functionalized magnetic nanoparticles as an efficient and recyclable catalyst for the one-pot production of biodiesel from grease via esterification and trans esterification, *Green Chem.* 16 (2014) 1202–1210, <https://doi.org/10.1039/C3GC41379A>.
- [54] Z.-J. Zhang, Y.-X. Wang, S.-L. Chou, H.-J. Li, H.-K. Liu, J.-Z. Wang, Rapid synthesis of $\alpha\text{-Fe}_2\text{O}_3/\text{rGO}$ nanocomposites by microwave autoclave as superior anodes for sodium-ion batteries, *J. Power Sources* 280 (2015) 107–113, <https://doi.org/10.1016/j.jpowsour.2015.01.092>.
- [55] M. Arunpandian, K. Selvakumar, A. Raja, P. Rajasekaran, M. Thirupathi, E. R. Nagarajan, S. Arunachalam, Fabrication of novel $\text{Nd}_2\text{O}_3/\text{ZnO-GO}$ nanocomposite: an efficient photocatalyst for the degradation of organic pollutants, *Colloids Surf. A: Physicochem. Eng. Asp.* 567 (2019) 213–227, <https://doi.org/10.1016/j.colsurfa.2019.01.058>.
- [56] F. Cardenas-Lizana, S. Gomez-Quero, N. Perret, M.A. Keane, Gold catalysis at the gas–solid interface: role of the support in determining activity and selectivity in the hydrogenation of m-dinitrobenzene, *Catal. Sci. Technol.* 1 (2011) 652–661, <https://doi.org/10.1039/C1CY00051A>.
- [57] A. Raja, K. Selvakumar, P. Rajasekaran, M. Arunpandian, S. Ashokkumar, K. Kaviyarasu, S. Asath Bahadur, M. Swaminathan, Visible active reduced graphene oxide loaded titania for photodecomposition of ciprofloxacin and its antibacterial activity, *Colloids Surf. A: Physicochem. Eng. Asp.* 564 (2019) 23–30, <https://doi.org/10.1016/j.colsurfa.2018.12.024>.
- [58] H.-L. Ma, Y. Zhang, Q.-H. Hu, D. Yan, Z.-Z. Yu, M. Zhai, Chemical reduction and removal of Cr(VI) from acidic aqueous solution by ethylenediamine-reduced graphene oxide, *J. Mater. Chem.* 22 (2012) 5914–5916, <https://doi.org/10.1039/C2JM00145D>.
- [59] J. Zielinski, I. Zglinicka, L. Znak, Z. Kaszkur, Reduction of Fe_2O_3 with hydrogen, *Appl. Catal. A: Gen.* 381 (2010) 191–196, <https://doi.org/10.1016/j.apcata.2010.04.003>.
- [60] F. Zhang, J. Zhang, H. Wang, J. Li, H. Liu, X. Jin, X. Wang, G. Zhang, Single tungsten atom steered band-gap engineering for graphitic carbon nitride ultrathin nanosheets boosts visible-light photocatalytic H_2 evolution, *Chem. Eng. J.* 424 (2021), 130004, <https://doi.org/10.1016/j.cej.2021.130004>.
- [61] Z. Feng, Q. Ma, J. Lu, H. Feng, J.W. Elam, P.C. Stair, M.J. Bedzyk, Atomic-scale cation dynamics in a monolayer $\text{VO}_x/\alpha\text{-Fe}_2\text{O}_3$ catalyst, *RSC Adv.* 5 (2015) 103834–103840, <https://doi.org/10.1039/C5RA18404E>.
- [62] L.H. Vieira, L.G. Possato, T.F. Chaves, S.H. Pulcinelli, C.V. Santilli, L. Martins, Studies on dispersion and reactivity of vanadium oxides deposited on lamellar ferrierite zeolites for condensation of glycerol into bulky products, *Mol. Catal.* 458 (2018) 161–170, <https://doi.org/10.1016/j.mcat.2017.11.027>.
- [63] R. Guo, X. Qi, X. Zhang, H. Zhang, X. Cheng, Synthesis of $\text{Ag}_2\text{CO}_3/\alpha\text{-Fe}_2\text{O}_3$ heterojunction and its high visible light driven photocatalytic activity for elimination of organic pollutants, *Sep. Purif. Technol.* 211 (18) (2019) 504–513, <https://doi.org/10.1016/j.seppur.2018.10.011>.
- [64] M. Arunpandian, K. Selvakumar, A. Raja, M. Thirupathi, P. Rajasekaran, P. Rameshkumar, E.R. Nagarajan, S. Arunachalam, Development of novel $\text{Nd}_2\text{WO}_6/\text{ZnO}$ incorporated on GO nanocomposite for the photocatalytic degradation of organic pollutants and biological studies, *J. Mater. Sci.: Mater. Electron.* 30 (20) (2019) 18557–18574, <https://doi.org/10.1007/s10854-019-02209-9>.
- [65] A. Raja, P. Rajasekaran, K. Selvakumar, M. Arunpandian, K. Kaviyarasu, S. Asath Bahadur, M. Swaminathan, Visible active reduced graphene oxide- $\text{BiVO}_4\text{-ZnO}$ ternary photocatalyst for efficient removal of ciprofloxacin, *Sep. Purif. Technol.* 233 (2020), 115996, <https://doi.org/10.1016/j.seppur.2019.115996>.
- [66] M. Zhao, Y. Cao, X. Liu, J. Deng, D. Li, H. Gu, Effect of nitrogen atomic percentage on N^+ -bombarded MWCNTs in cytocompatibility and hemocompatibility, *Nanoscale Res. Lett.* 9 (2014) 142, <https://doi.org/10.1186/1556-276X-9-142>.
- [67] W.-J. Li, S.-L. Chou, J.-Z. Wang, H.-K. Liu, S.-X. Dou, Significantly enhance the cycling performance and rate capability for P/C composite via chemical bonding (P–C), *J. Mater. Chem. A* 4 (2016) 505–511, <https://doi.org/10.1039/C5TA08590J>.
- [68] Y. Zhu, J. Li, C.-L. Dong, J. Ren, Y.-C. Huang, D. Zhao, R. Cai, D. Wei, X. Yang, C. Lv, W. Theis, Y. Bu, W. Han, S. Shen, D. Yang, Red phosphorus decorated and doped TiO_2 nanofibers for efficient photocatalytic hydrogen evolution from pure water, *Appl. Catal. B: Environ.* 255 (2019), 117764, <https://doi.org/10.1016/j.apcatb.2019.117764>.
- [69] J. Liu, Y. Zhu, J. Chen, D.S. Butenko, J. Ren, X. Yang, P. Lu, P. Meng, Y. Xu, D. Yang, S. Zhang, Visible-light driven rapid bacterial inactivation on red phosphorus/titanium oxide nanofiber heterostructures, *J. Hazard. Mater.* 413 (2021), 125462, <https://doi.org/10.1016/j.jhazmat.2021.125462>.
- [70] J. Huang, D. Li, R. Li, Q. Zhang, T. Chen, H. Liu, Y. Liu, W. Lv, G. Liu, An efficient metal-free phosphorus and oxygen co-doped g- C_3N_4 photocatalyst with enhanced visible light photocatalytic activity for the degradation of fluoroquinolone antibiotics, *Chem. Eng. J.* 374 (2019) 242–253, <https://doi.org/10.1016/j.cej.2019.05.175>.
- [71] K. Jiratova, A. Spojakina, J. Balabanova, R. Palcheva, G. Tyuliev, Y. Karakirova, Deep oxidation of ethanol over SiO_2 -supported MoV heteropoly acids modified with palladium, *React. Kinet. Mech. Catal.* 125 (2018) 901–922, <https://doi.org/10.1007/s1144-018-1462-5>.
- [72] A. Uheida, A. Mohamed, M. Belaqiz, W.S. Nasser, Photocatalytic degradation of Ibuprofen, Naproxen, and Cetirizine using PANMWNT nanofibers crosslinked $\text{TiO}_2\text{-NH}_2$ nanoparticles under visible light irradiation, *Sep. Purif. Technol.* 212 (2018) 110–118, <https://doi.org/10.1016/j.seppur.2018.11.030>.
- [73] A. Nunez-Flores, A. Sandoval, E. Mancilla, A. Hidalgo-Millan, G. Ascanio, Enhancement of photocatalytic degradation of ibuprofen contained in water using a static mixer, *Chem. Eng. Res. Des.* 156 (2020) 54–63, <https://doi.org/10.1016/j.cherd.2020.01.018>.
- [74] W. Cao, Y. Yuan, C. Yang, S. Wu, J. Cheng, In-situ fabrication of g- $\text{C}_3\text{N}_4/\text{MIL-68}(\text{In})\text{-NH}_2$ heterojunction composites with enhanced visible-light photocatalytic activity for degradation of ibuprofen, *Chem. Eng. J.* 391 (2020), 123608, <https://doi.org/10.1016/j.cej.2019.123608>.
- [75] S.-H. Liu, W.-T. Tang, P.-H. Chou, Microwave-assisted synthesis of triple 2D g- $\text{C}_3\text{N}_4/\text{Bi}_2\text{WO}_6/\text{rGO}$ composites for ibuprofen photodegradation: kinetics, mechanism and toxicity evaluation of degradation products, *Chem. Eng. J.* 387 (2020), 124098, <https://doi.org/10.1016/j.cej.2020.124098>.
- [76] A. Gomez-Aviles, M. Penas-Garzon, J. Bedia, D.D. Dionysiou, J.J. Rodriguez, C. Belver, Mixed Ti-Zr metal-organic-frameworks for the photodegradation of acetaminophen under solar irradiation, *Appl. Catal. B Environ.* 253 (2019) 253–262, <https://doi.org/10.1016/j.apcatb.2019.04.040>.
- [77] M. Guo, Z. Zhou, S. Yan, P. Zhou, F. Miao, S. Liang, J. Wang, X. Cui, $\text{Bi}_2\text{WO}_6\text{-BiOCl}$ heterostructure with enhanced photocatalytic activity for efficient degradation of oxytetracycline, *Sci. Rep.* 10 (2020) 18401, <https://doi.org/10.1038/s41598-020-75003-x>.
- [78] L. Yu, Y. Shao, D. Li, Direct combination of hydrogen evolution from water and methane conversion in a photocatalytic system over Pt/TiO_2 , *Appl. Catal. B Environ.* 204 (2017) 216–223, <https://doi.org/10.1016/j.apcatb.2016.11.039>.
- [79] Z. Zhu, Z. Lu, D. Wang, X. Tang, Y. Yan, W. Shi, Y. Wang, N. Gao, X. Yao, H. Dong, Construction of high-dispersed $\text{Ag}/\text{Fe}_3\text{O}_4/\text{g-C}_3\text{N}_4$ photocatalyst by selective photo-deposition and improved photocatalytic activity, *Appl. Catal. B Environ.* 182 (2016) 115–122, <https://doi.org/10.1016/j.apcatb.2015.09.029>.
- [80] C. Gao, J. Low, R. Long, T. Kong, J. Zhu, Y. Xiong, Heterogeneous single-atom photocatalysts: fundamentals and applications, *Chem. Rev.* 120 (2020) 12175–12216, <https://doi.org/10.1021/acs.chemrev.9b00840>.
- [81] T. Shanmugaprabha, K. Selvakumar, K. Rajasekaran, P. Sami, A kinetic study of the oxidations of 2-mercaptoethanol and 2-mercaptoethylamine by heteropoly 11-tungsto-1-vanadophosphate in aqueous acidic medium, *Transit. Met. Chem.* 41 (2016) 77–85, <https://doi.org/10.1007/s11243-015-9998-y>.
- [82] Z. Chen, X. Chu, X. Huang, H. Sun, L. Chen, F. Guo, Fabrication of visible-light driven $\text{CoP}/\text{ZnSnO}_3$ composite photocatalyst for high-efficient photodegradation of antibiotic pollutant, *Sep. Purif. Technol.* 257 (2021), 117900, <https://doi.org/10.1016/j.seppur.2020.117900>.
- [83] Y. Zheng, Y. Liu, X. Guo, Z. Chen, W. Zhang, Y. Wang, X. Tang, Y. Zhang, Y. Zhao, Sulfur-doped g- $\text{C}_3\text{N}_4/\text{rGO}$ porous nanosheets for highly efficient photocatalytic degradation of refractory contaminants, *J. Mater. Sci. Technol.* 41 (2020) 117–126, <https://doi.org/10.1016/j.jmst.2019.09.018>.
- [84] D. Liu, P. Zhu, L. Yin, X. Zhang, K. Zhu, J. Tan, R. Jin, Facile fabrication of $\text{Bi}_2\text{GeO}_5/\text{Ag}/\text{Ag}_3\text{PO}_4$ for efficient photocatalytic RhB degradation, *J. Solid State Chem.* 301 (2021), 122309, <https://doi.org/10.1016/j.jssc.2021.122309>.
- [85] J. Choina, H. Kosslick, Ch Fischer, G.-U. Flechsig, L. Frunza, A. Schulz, Photocatalytic decomposition of pharmaceutical ibuprofen pollutants in water over titania catalyst, *Appl. Catal. B* 129 (2013) 589–598, <https://doi.org/10.1016/j.apcatb.2012.09.053>.